Journal of Computational Physics 229 (2010) 828–850

Contents lists available at ScienceDirect

Journal of Computational Physics

journal homepage: www.elsevier.com/locate/jcp

Implicit LU-SGS algorithm for high-order methods on unstructured grid with *p*-multigrid strategy for solving the steady Navier–Stokes equations

M. Parsani [a,*], K. Van den Abeele [a], C. Lacor [a], E. Turkel [b]

[a] Vrije Universiteit Brussel, Department of Mechanical Engineering, Fluid Dynamics and Thermodynamics Research Group, Pleinlaan 2, 1050 Brussel, Belgium
[b] Tel-Aviv University, Department of Mathematics, Tel-Aviv, Ramat Aviv 69978, Israel

ARTICLE INFO

Article history:
Received 4 December 2008
Received in revised form 6 October 2009
Accepted 9 October 2009
Available online 17 October 2009

Keywords:
Navier–Stokes
High-order methods
Implicit LU-SGS algorithm
Von Neumann analysis
p-Multigrid

ABSTRACT

The fluid dynamic equations are discretized by a high-order spectral volume (SV) method on unstructured tetrahedral grids. We solve the steady state equations by advancing in time using a backward Euler (BE) scheme. To avoid the inversion of a large matrix we approximate BE by an implicit lower–upper symmetric Gauss–Seidel (LU-SGS) algorithm. The implicit method addresses the stiffness in the discrete Navier–Stokes equations associated with stretched meshes. The LU-SGS algorithm is then used as a smoother for a *p*-multigrid approach. A Von Neumann stability analysis is applied to the two-dimensional linear advection equation to determine its damping properties. The implicit LU-SGS scheme is used to solve the two-dimensional (2D) compressible laminar Navier–Stokes equations. We compute the solution of a laminar external flow over a cylinder and around an airfoil at low Mach number. We compare the convergence rates with explicit Runge–Kutta (E-RK) schemes employed as a smoother. The effects of the cell aspect ratio and the low Mach number on the convergence are investigated. With the *p*-multigrid method and the implicit smoother the computational time can be reduced by a factor of up to 5–10 compared with a well tuned E-RK scheme.

1. Introduction

Spatially high-order accurate numerical schemes are being developed for use in a variety of flow problems. In Computational Fluid Dynamics (CFD), they are being used for Direct Numerical Simulation (DNS), Large Eddy Simulation (LES), Computational Aeroacoustics (CAA), turbulent combustion etc. where the accurate resolution of small scales is required. In addition, since CFD is increasingly used as an industrial design and analysis tool, it requires unstructured grids for efficient meshing. High-order accuracy must therefore be achieved on unstructured grids. Discontinuous Galerkin (DG) schemes [1–5], Residual Distribution (RDS) [6] and the more recently developed Spectral Volume (SV) [7–15] and Spectral Difference (SD) [17–19] schemes are especially suited for these purposes.

However, when high-order schemes are combined with classical solution methods, such as explicit Runge–Kutta (E-RK) solvers, they suffer from a restrictive CFL condition and hence a relatively slow convergence rate. In addition to this, the solver must also be able to deal with the geometrical stiffness imposed by the Navier–Stokes grids where high-aspect ratios

* Corresponding author. Tel.: +32 2 6292399; fax: +32 2 6292880.
E-mail addresses: mparsani@vub.ac.be (M. Parsani), kvdabeel@vub.ac.be (K. Van den Abeele), chris.lacor@vub.ac.be (C. Lacor), turkel@post.tau.ac.il (E. Turkel).

0021-9991/$ - see front matter © 2009 Elsevier Inc. All rights reserved.
doi:10.1016/j.jcp.2009.10.014

occur near walls. In the case of compressible solvers there is an additional stiffness when solving for low speed flows caused by the disparate eigenvalues of the system.

High-order schemes possess less numerical dissipation than the lower-order ones. Consequently, it takes an excessive amount of CPU-time to reach a steady-state solution with explicit solvers. Therefore, efficient solvers are needed to fully fulfill the potential of high-order methods. Implicit time-integration schemes can be used to deal with these problems. These schemes can advance the solution with significantly larger time-steps compared to explicit methods. However, they may be more expensive than explicit schemes if the algebraic solver employed is not efficient. Recently, there has been some research on implicit Runge–Kutta (I-RK) schemes [20,21]. In Bijl et al. [20], I-RK solvers were investigated in combination with a standard cell-centered finite volume scheme with artificial dissipation added for stability. It was observed that significant potential improvements in the temporal efficiency of implicit schemes could be achieved from algebraic solver developments. In [21] the convergence of an E-RK scheme with *h*-multigrid was accelerated by preconditioning with a fully implicit operator and the resulting RK/Implicit Residual scheme was used as a smoother for an *h*-multigrid algorithm. It was demonstrated that the implicit preconditioner reduced the computational time of a well tuned E-RK scheme by a factor between 4 and 10. Both studies [20,21], concluded that solver improvements can be more dramatic than improvements in integration techniques.

Another indispensable tool for efficiency is the multigrid algorithm. In the traditional *h*-multigrid approach, efficiency is achieved by switching to coarser spatial grids. In a *p*-multigrid algorithm, a high-order solution representation is transferred to a lower-order one and the multigrid algorithm uses iterations on sequences of different solution representations instead of different grids. Essential for efficiency is that the solver is a good smoother of high-frequency error components and this should also hold for high-aspect ratio grids.

In the present study we combine a SV discretization in space and an implicit lower–upper symmetric Gauss–Seidel (LU-SGS) in (pseudo) time. This is accelerated by a full *p*-multigrid strategy. The LU scheme was started by Jameson and Turkel [22] and later reformulated to use symmetric Gauss–Seidel by Jameson and Yoon in the context of second-order central schemes [23]. It was recently rediscovered by Sun et al. [24] and adapted for use with SD schemes. In Parsani et al. [27] it was coupled with the SV scheme and a full *p*-multigrid algorithm. Here, the LU-SGS algorithm with the backward Euler method is evaluated both with analysis and computation. The damping properties of the implicit method are evaluated with a Von Neumann stability analysis for a model 2D linear advection equation. In [25,26] this analysis was applied to implicit schemes on Cartesian grids for classical upwind and central schemes. In the present work the analysis is on triangular grids defined by a generating pattern, and for high-order SV schemes.

The implicit LU-SGS scheme is used to solve the two-dimensional steady laminar flows over a cylinder and a NACA0012 airfoil at low Mach number. For the two cases the order of the SV scheme is restricted to 2 because of the curved boundaries. Currently a first-order interpolation is used for the boundary shape. High-order schemes, would require a more accurate interpolation, especially on the relatively coarse grids that are being used in combination with high-order schemes [13].

The convergence behavior and the computational effort of the implicit LU-SGS algorithm is compared with that of a family of optimized E-RK smoothers used in Van den Abeele et al. [14]. The influence of the mesh aspect ratio and the low Mach number is investigated and the solutions are compared with experimental and numerical results found in the literature. For the NACA0012 airfoil test case the convergence behavior of the LU-SGS solver is compared with that of RK/Implicit Residual scheme used in [21]. The latter code is second-order accurate in space and uses a finite volume approach with quadrilateral cells on structured grids.

The remainder of this article is organized as follows. A brief summary of the SV method is given in section 2. In Section 3, the *p*-multigrid algorithm is described with the definition of a general restriction operator [27]. In Section 4, the explicit Runge–Kutta schemes (E-RK) are described. In Section 5, the implicit LU-SGS with backward Euler (BE) scheme is discussed. A Von Neumann stability analysis for the LU-SGS with backward Euler method and for a general SV schemes on triangular grids is described in Section 6. Section 7 shows the stability analysis' results for the second-order SV scheme. Section 8 deals with the numerical test cases, before finally drawing conclusions in Section 9.

2. Spectral volume method

The spectral volume (SV) method is used to solve conservation laws (1)

$$\frac{\partial \mathbf{W}}{\partial t} + \nabla \cdot \mathcal{F}(\mathbf{W}) = 0, \tag{1}$$

where $\mathbf{W}$ is the state vector of conservative variables and $\mathcal{F}(\mathbf{W})$ is the flux density tensor.

The computational domain V is divided in N^{SV} cells V_i, called spectral volumes, with volume $|V_i|$. Each SV is further subdivided into control volumes (CV) V_{ij}. Integrating Eq. (1) over such a CV and applying the Gauss theorem gives

$$\frac{\partial}{\partial t}\left(\overline{W}_{ij}|V_{ij}|\right) = -\int_{\partial V_{ij}} \mathcal{F} \cdot d\mathbf{s} = R_{ij}, \tag{2}$$

where $|V_{ij}|$ is the volume of V_{ij}, R_{ij} is the residual corresponding to V_{ij} and $\overline{W}_{ij}$ is the CV average defined by

$$\overline{W}_{i,j} \equiv \frac{1}{|V_{i,j}|}\int_{V_{i,j}} \mathbf{W}\, dV. \tag{3}$$

On a spectral volume V_i, the SV polynomial approximation of the solution is defined as

$$W_{V_i} \approx w_{V_i} \equiv \sum_{j=1}^{N^{CV}(p,d)} \overline{W}_{i,j}\overline{L}_{i,j}. \tag{4}$$

In Eq. (4), $N^{CV}(p,d)$ is the number of CVs in a SV, which depends on the desired degree of the polynomial approximation p and the number of spatial dimensions d. The polynomials $\overline{L}_{i,j}$ associated to the CVs $V_{i,j}$ are defined by

$$\frac{1}{|V_{i,j}|}\int_{V_{i,j}} \overline{L}_{i,m} dV = \delta_{jm}, \tag{5}$$

where δ_{jm} is the Kronecker delta function. With the polynomial approximation w_{V_i}, the flux integral in Eq. (2) can be approximated to order $p+1$, using Gauss quadrature. On the boundary between two SVs however, there are two available values for the flux $\mathcal{F}$, one from within each SV. Thus, on these boundaries a suitable numerical Riemann flux $\mathbf{F}$, for instance the Rusanov flux [28] or the Roe flux [29], must be used. A more elaborate overview of the SV method can be found in [7–15]. In this study the computation of the inviscid fluxes follows the classical approach described in [7–12], while the computation of the viscous fluxes is based on the local DG idea [5]. Fig. 1 shows three 2D SV partitions that correspond to, from left to right, a second (SV2), a third (SV3) and a fourth-order (SV4) accurate SV scheme. The SV2 partition has three CVs and is uniquely defined. A SV3 contains six CVs and the partition has two degrees of freedom, namely $\alpha_3 = \frac{|AB|}{|AE|}$ and $\beta_3 = \frac{|AC|}{|AD|}$. The SV4 partition consists of ten CVs and has four degrees of freedom. These are $\alpha_4 = \frac{|AB|}{|AG|}$, $\beta_4 = \frac{|AC|}{|AF|}$, $\gamma_4 = \frac{|EF|}{|AF|}$ and $\delta_4 = \frac{|AD|}{|AF|}$. The accuracy and stability properties strongly depend on the choice of these parameters and their effects are analyzed in [15].

3. *p*-Multigrid algorithm

The main idea of multigrid is based on the observation that error-smoothing operators are generally efficient in eliminating high-frequency errors, but less adequate for the low-frequency errors. The multigrid strategy is to switch to a coarser representation of the solution, where the low-frequency errors of the fine representation occur as high-frequency modes, which can thus be efficiently damped out. In the traditional h-multigrid approach, this is done by switching to a coarser spatial grid. With a p-multigrid algorithm, a high-order solution representation is transferred to a lower-order one.

A two-level Full Approximation Scheme algorithm (FAS), as proposed by Brandt [16], can be summarized in the following way. To solve a fine level problem $\mathbf{R}^f(\overline{\mathbf{U}}^f) = 0$, perform the following operations:

- Perform ν_1 smoothing sweeps on the fine level: $\overline{\mathbf{W}}^f \leftarrow (\mathbf{G}^f)^{\nu_1}\overline{\mathbf{W}}^f$.
- Transfer the state and the residual to the coarse level: $\overline{\mathbf{W}}_0^c \leftarrow \widetilde{I}_f^c\overline{\mathbf{W}}^f$, $\mathbf{f}^c \leftarrow \mathbf{R}^c(\overline{\mathbf{W}}^f) - \mathbf{R}^c(\overline{\mathbf{W}}_0^c) = I_f^c\mathbf{R}^f(\overline{\mathbf{W}}^f) - \mathbf{R}^c(\overline{\mathbf{W}}_0^c)$.
- Solve the coarse level problem: $\mathbf{R}^c(\overline{\mathbf{W}}^c) = \mathbf{f}^c$.
- Prolongate the coarse level error and correct the fine level state: $\overline{\mathbf{W}}^f \leftarrow \overline{\mathbf{W}}^f + I_c^f(\overline{\mathbf{W}}^c - \overline{\mathbf{W}}_0^c)$.
- Perform ν_2 smoothing sweeps on the fine level: $\overline{\mathbf{W}}^f \leftarrow (\mathbf{G}^f)^{\nu_2}\overline{\mathbf{W}}^f$.

In this algorithm, $\mathbf{G}^f$ represents an arbitrary smoothing operator on the fine level and in this work it is the implicit LU-SGS algorithm coupled with the BE scheme. $\mathbf{f}^c$ is the so-called forcing function. The coarse level problem can again be solved using a FAS algorithm, and so on. In this way, one arrives at a V-cycle. A further increase in efficiency can be achieved by initializing the solution on coarser levels (Full Multigrid Algorithm). In this way, a better initial solution is provided for the fine levels, which will also improve the robustness of the method. In the present paper, the switch to a finer level is made when the L_2 norm of the coarse level residuals is smaller than a factor η_{switch} times the L_2 norm of the fine level residual and η_{switch} is set to 0.001.

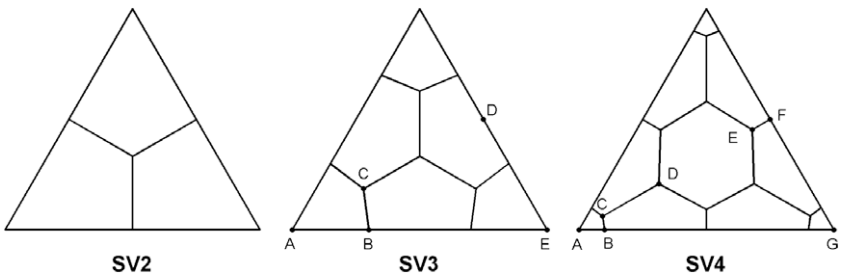

Fig. 1. Spectral volume partitions.

The p-multigrid algorithm for a SV method, employed here, is largely based on the algorithm used by Van den Abeele et al. [14] where the prolongation (I_c^f) and the state restriction ($\widetilde{I}_f^c$) operators, with omission of the SV index i, are defined as follow:

- Prolongation operator: the coarse level polynomials L_j^c can be written as a function of the fine level polynomials L_m^f:

$$L_j^c = \sum_{m=1}^{N_f} \alpha_{jm} L_m^f \quad j = 1, \ldots, N_c, \tag{6}$$

  where N_c and N_f are the number of CVs within a SV on the coarse and fine levels. By equating the fine level solution to the coarse level solution, the following expression for I_c^f is found: $(I_c^f)_{mj} \equiv \alpha_{jm}$.
- State restriction operator: this operator can also be defined by projecting the fine level solution onto the coarse level polynomial basis. This results in the following definition for $\widetilde{I}_f^c : (\widetilde{I}_f^c)_{mj} = (P^{-1}Q)_{mj}$. The matrices P and Q are defined by

$$P_{jm} = \int_V L_j^c L_m^c dV \quad j, m = 1, \ldots, N_c, \tag{7}$$

$$Q_{jm} = \int_V L_j^c L_m^f dV \quad j = 1, \ldots, N_c \; m = 1, \ldots, N_f. \tag{8}$$

The residual restriction operator used in this paper is more general than the one that was used in Van den Abeele et al. [14], and is valid for any 2D or 3D cell, [27]. It is based on the idea that the residuals (after dividing them by the CV volume, just like the solution) are also CV-averaged quantities. Therefore, the residual restriction operator is defined as:

$$\left(I_f^c\right)_{ij} \equiv V_j^c \left(\widetilde{I}_f^c\right)_{jk} \frac{1}{V_k^f}. \tag{9}$$

4. Explicit Runge–Kutta schemes

In the present work, the results obtained with the implicit LU-SGS are compared with those obtained with the E-RK smoothers used in Van den Abeele et al. [14]. Explicit N_{RK}-stage (E-RK) schemes of the following form are employed:

$$\overline{W}_{i,j}^0 = \overline{W}_{i,j}^n,$$

$$\overline{W}_{i,j}^m = C_m^1 \overline{W}_{i,j}^0 + C_m^2 \overline{W}_{i,j}^{m-1} + C_m^3 \frac{\Delta t}{|V_{i,j}|} R_{i,j}^{m-1} \quad 1 \leqslant m \leqslant N_{RK},$$

$$\overline{W}_{i,j}^{n+1} = \overline{W}_{i,j}^{N_{RK}}.$$

where the coefficients C_m^1, C_m^2, C_m^3 are listed in Table 1.

5. Implicit LU-SGS algorithm

Consider the semi-discretization of a system of conservation equations:

$$\frac{\partial \mathbf{W}}{\partial t} - \mathbf{R}(\mathbf{W}(t)) = 0, \tag{10}$$

where $\mathbf{R}(\cdot)$ is a vector operator whose components are spatial difference operators representing a discrete approximation for $\nabla \cdot \mathcal{F}(\mathbf{W})$ in Eq. (1). Approximate the temporal derivative with the backward Euler (BE) algorithm

$$\frac{\mathbf{W}^{n+1} - \mathbf{W}^n}{\Delta t} - \left[\mathbf{R}\left(\mathbf{W}^{n+1}\right) - \mathbf{R}(\mathbf{W}^n)\right] = \mathbf{R}(\mathbf{W}^n), \tag{11}$$

where Δt is the time step and the superscripts n and $n+1$ denote time levels. Assume that the computational domain is subdivided into cells. Apply Eq. (11) to a single cell denoted by the subscript c (for the SV method c corresponds to one spectral volume),

Table 1
Coefficients of the different E-RK schemes. Index m takes the values $1, \ldots, N_{RK}$.

Scheme	C_m^1	C_m^2	C_1^3	C_2^3	C_3^3	C_4^3	C_5^3
opt RK2	1	0	$\frac{1}{4}$	1	–	–	–
opt RK3	1	0	$\frac{1}{5}$	$\frac{1}{2}$	1	–	–
opt RK5	1 (if $m = 1$)	0 (if $m = 1$)	$\frac{85}{1300}$	$\frac{1}{10}$	$\frac{9}{50}$	$\frac{1}{4}$	$\frac{132}{300}$
	$1 - C_m^3$ (if $m \neq 1$)	C_m^3 (if $m \neq 1$)					

$$\frac{\mathbf{W}_c^{n+1}-\mathbf{W}_c^n}{\Delta t}-\left[\mathbf{R}\left(\mathbf{W}_c^{n+1}\right)-\mathbf{R}\left(\mathbf{W}_c^n\right)\right]=\mathbf{R}\left(\mathbf{W}_c^n\right). \tag{12}$$

Let $\Delta\mathbf{W}_c=\mathbf{W}_c^{n+1}-\mathbf{W}_c^n$. Linearizing the residual using the Taylor expansion about $\mathbf{W}_c^n$ gives

$$\mathbf{R}_c(\mathbf{W}^{n+1})-\mathbf{R}_c(\mathbf{W}^n)\approx\frac{\partial\mathbf{R}_c}{\partial\mathbf{W}_c}\Delta\mathbf{W}_c+\sum_{nb\neq c}\frac{\partial\mathbf{R}_c}{\partial\mathbf{W}_{nb}}\Delta\mathbf{W}_{nb}, \tag{13}$$

where *nb* indicates all the neighboring cells contributing to the residual of cell *c*. Therefore, the fully linearized equations for (12) can be written as

$$\left(\frac{\mathbf{I}}{\Delta t}-\frac{\partial\mathbf{R}_c}{\partial\mathbf{W}_c}\right)\Delta\mathbf{W}_c-\sum_{nb\neq c}\frac{\partial\mathbf{R}_c}{\partial\mathbf{W}_{nb}}\Delta\mathbf{W}_{nb}=\mathbf{R}_c(\mathbf{W}^n), \tag{14}$$

where $\mathbf{I}$ is the identity matrix. However, Eq. (14) requires too much memory to store the LHS implicit Jacobian matrices. Therefore, the most recent solution for the *nb* cells is used [24],

$$\left(\frac{\mathbf{I}}{\Delta t}-\frac{\partial\mathbf{R}_c}{\partial\mathbf{W}_c}\right)\Delta\mathbf{W}_c^{(k+1)}=\mathbf{R}_c\left(bfW^n\right)+\sum\nolimits_{nb\neq c}\frac{\partial\mathbf{R}_c}{\partial bfW_{nb}}\Delta\mathbf{W}_{nb}^{(*)}, \tag{15}$$

with superscript * denoting the most recent solution when doing forward and backward sweeps. Superscript $k+1$ refers to the actual SGS sweep, i.e. $\Delta\mathbf{W}_c^{(k+1)}=\mathbf{W}_c^{n+1,(k+1)}-\mathbf{W}_c^n$.

In [21], Eq. (15) is solved with a first-order upwind scheme with the Jacobians calculated each time step and not stored. However, this may not be an efficient solution because the computation of the $\frac{\partial\mathbf{R}_c}{\partial\mathbf{W}_{nb}}$ for high-order method is time-consuming. Hence, to avoid the computation and the storage of the off-diagonal block matrices, expression (15) is further manipulated as follows [24]:

$$\mathbf{R}_c(\mathbf{W}^n)+\sum_{nb\neq c}\frac{\partial\mathbf{R}_c}{\partial\mathbf{W}_{nb}}\Delta\mathbf{W}_{nb}^{(*)}\approx\mathbf{R}_c\left(\mathbf{W}_c^{(*)},\left\{\mathbf{W}_{nb}^{(*)}\right\}\right)-\frac{\partial\mathbf{R}_c}{\partial\mathbf{W}_c}\Delta\mathbf{W}_c^{(*)}=\mathbf{R}_c\left(\mathbf{W}^{(*)}\right)-\frac{\partial\mathbf{R}_c}{\partial\mathbf{W}_c}\Delta\mathbf{W}_c^{(*)}. \tag{16}$$

Let $\widetilde{\Delta\mathbf{W}}_c^{(k+1)}\equiv\Delta\mathbf{W}_c^{(k+1)}-\Delta\mathbf{W}_c^{(*)}=\mathbf{W}_c^{n+1,(k+1)}-\mathbf{W}_c^{n+1,(*)}$. Consequently, combining Eqs. (16) and (15) the final Eq. (17)

$$\left(\frac{\mathbf{I}}{\Delta t}-\frac{\partial\mathbf{R}_c}{\partial\mathbf{W}_c}\right)\widetilde{\Delta\mathbf{W}}_c^{(k+1)}=\mathbf{R}_c\left(\mathbf{W}^{(*)}\right)-\frac{\Delta\mathbf{W}_c^{(*)}}{\Delta t}. \tag{17}$$

The linear system (17) is solved with multiple cell-wise symmetric forward and backward sweeps with a prescribed tolerance on the change $\widetilde{\Delta\mathbf{W}}_c^{(k+1)}$ and/or a maximum number of symmetric forward and backward sweeps. This implicit solver is denoted as 'LU-SGS + BE' in the remainder of this paper, where BE stands for backward Euler scheme. Note that solving Eq. (17) to machine zero implies that Eq. (12) is satisfied, i.e. the nonlinear system of equations is solved exactly. Moreover, if Eq. (12) is satisfied and the CFL number is smaller or equal to one, than the implicit LU-SGS is actually a physical time-advancing scheme.

The initial guess for $\mathbf{W}_c^{n+1}$ is $\mathbf{W}_c^n$. In the present work, the L_2 norm of the solution variation or RHS of Eq. (17) are monitored for convergence. For steady state problems, it is not necessary to drive the RHS of Eq. (17) to machine zero, but it is more efficient to limit the maximum number of SGS sweeps to damp high-frequency error components and/or set a threshold for some norm of the change $\widetilde{\Delta\mathbf{W}}_c^{(k+1)}$. More details about the values of the parameters used to solve the system (17) are given in Section 8.

The term $\Delta\mathbf{W}_c^{(*)}$ in the RHS of Eq. (17) introduces an under-relaxation effect because it is influenced by the solution computed several sweeps before, [30]. Therefore, neglecting $\Delta\mathbf{W}_c^{(*)}$ may accelerate the convergence. However, the aim of the present paper is the analysis of the damping properties of the original implicit LU-SGS algorithm proposed in Sun et al. [24] and unless otherwise stated, the results of the Sections 6 and 8 refer to the original algorithm where the term $\Delta\mathbf{W}_c^{(*)}/\Delta t$, in the RHS of Eq. (17) is taking into account. Notice that the present approach requires less memory than fully implicit methods since only the block matrices on the diagonal of the system matrix are stored.

6. Von Neumann stability analysis

The objective of this section is to evaluate the LU-SGS + BE scheme as a smoother for a multigrid method using the Von Neumann stability analysis. In [25,26] this analysis was applied to implicit schemes on Cartesian grids for classical upwind and central scheme. We present the analysis on triangular grids, defined by a generating pattern, and for a general SV schemes. The Von Neumann stability analysis is applied to the 2D linear advection equation on a domain with periodic boundary conditions, [15]:

$$\frac{\partial v}{\partial t}+a_x\frac{\partial v}{\partial x}+a_y\frac{\partial v}{\partial y}=0, \tag{18}$$

$$\mathbf{a}=\left[a_x a_y\right]^T=a[\cos\psi\ \sin\psi]^T=a\mathbf{1}_a. \tag{19}$$

The vector $\mathbf{a}$ is the wave propagation velocity with Cartesian components a_x and a_y, or amplitude a and the direction given by the angle ψ. The initial solution is a harmonic plane wave, with wave number k and orientation defined by the angle θ:

$$v(x,y,t_0) = v(x,y,0) = e^{Ik(x\cos\theta + y\sin\theta)}, \tag{20}$$

where $I = \sqrt{-1}$. A $(p+1)$th-order accurate SV method is applied to (18), on a mesh whose generating pattern is shown in Fig. 2. This generating pattern consists of two triangular SVs (SV_1 and SV_2) which are periodically repeated to form the real mesh. The generating pattern is completely defined by the vectors $\mathbf{B}_1 = [B_{1x}\, B_{1y}]^T$ and $\mathbf{B}_2 = [B_{2x}\, B_{2y}]^T$ and their non-dimensional form is obtained by scaling them with the length of $\mathbf{B}_1$, denoted by $\Delta B : \mathbf{B}_1 \equiv \Delta B \mathbf{B}'_1$ and $\mathbf{B}_2 \equiv \Delta B \mathbf{B}'_2$. On the boundary between two SVs, the following Riemann flux is used:

$$\mathbf{F}^R\left(v^L, v^R\right)\cdot \mathbf{1}_n = \frac{\mathbf{a}\cdot\mathbf{1}_n\left(v^L + v^R\right)}{2} - \varphi\frac{|\mathbf{a}\cdot\mathbf{1}_n|\left(v^R - v^L\right)}{2}, \tag{21}$$

where v^L is the solution of the left cell on the face and v^R the one of the right cell on the face. The normal to the face $\mathbf{1}_n$ points into the right cell. φ is an upwinding parameter, where $\varphi = 1$ results in a simple upwind flux and $\varphi = 0$ gives a central flux. After application of the SV method to (18), the following equations is obtained:

$$\begin{aligned}\Delta B^2 \sum_{l=1}^{2N^{CV}} Q_{m,l}\frac{d\bar{v}_{i,j;l}}{dt} + a\Delta B\sum_{l=1}^{2N^{CV}} A^0_{m,l}\bar{v}_{i,j;l} + a\Delta B\sum_{l=1}^{2N^{CV}} A^{-1}_{m,l}\bar{v}_{i-1,j;l} + a\Delta B\sum_{l=1}^{2N^{CV}} A^{+1}_{m,l}\bar{v}_{i+1,j;l} + a\Delta B\sum_{l=1}^{2N^{CV}} C^{-1}_{m,l}\bar{v}_{i,j-1;l}\\ + a\Delta B\sum_{l=1}^{2N^{CV}} C^{+1}_{m,l}\bar{v}_{i,j+1;l} = 0,\end{aligned} \tag{22}$$

where $N^{CV} = (p+1)(p+2)/2$ is the number of CVs in each SV. The index m takes the values $1,\ldots,2N^{CV}$. Indices i and j are the generating pattern indices. The variables $\bar{v}_{i,j,l}$ for $l = 1,\ldots,N^{CV}$ are the CV-averaged values in the first SV of the generating pattern (marked SV_1 in Fig. 2), while the variables for $l = N^{CV}+1,\ldots,2N^{CV}$ correspond to the CV-averaged values of the second SV (marked SV_2). The matrices $Q_{m,l}$, $A^0_{m,l}$, $A^{-1}_{m,l}$, $A^{+1}_{m,l}$, $C^{-1}_{m,l}$ and $C^{+1}_{m,l}$ are a function of the wave propagation direction ψ and their definitions are included in the Appendix of Van den Abeele et al. [15]. The factor ΔB is used to make these matrices and V' dimensionless. ΔB^2 is the area of the triangles divided by the dimensionless volume V' of the SV which is given by $V' = |\mathbf{B}_1 \times \mathbf{B}_2|/(2\Delta B^2)$.

Approximating the time derivative in Eq. (22) with a backward Euler scheme Eq. (23) is obtained,

$$\bar{\mathbf{v}}^{n+1}_{i,j} - \bar{\mathbf{v}}^{n}_{i,j} + \sigma\mathbf{M}^0\bar{\mathbf{v}}^{n+1}_{i,j} + \sigma\mathbf{M}^{-1}\bar{\mathbf{v}}^{n+1}_{i-1,j} + \sigma\mathbf{M}^{+1}\bar{\mathbf{v}}^{n+1}_{i+1,j} + \sigma\mathbf{N}^{-1}\bar{\mathbf{v}}^{n+1}_{i,j-1} + \sigma\mathbf{N}^{+1}\bar{\mathbf{v}}^{n+1}_{i,j+1} = 0, \tag{23}$$

where $\sigma = \frac{a\Delta t}{\Delta B}$, $\mathbf{v}_{i,j}$ and n represent respectively, the CFL number, the variables of the generating pattern and the time iteration index. The matrices $\mathbf{M}^0$, $\mathbf{M}^{-1}$, $\mathbf{M}^{+1}$, $\mathbf{N}^{-1}$ and $\mathbf{N}^{+1}$ are computed multiplying the matrices $\mathbf{A}^0$, $\mathbf{A}^{-1}$, $\mathbf{A}^{+1}$, $\mathbf{C}^{-1}$ and $\mathbf{C}^{+1}$ with the matrix $(V'\mathbf{Q})^{-1}$.

The linear system (23) may also be written in a more compact form, i.e.

$$\mathbf{E}\bar{\mathbf{v}}^{n+1} = \bar{\mathbf{v}}^{n}, \tag{24}$$

where the matrix $\mathbf{E}$ is obtained by assembling the matrices $\mathbf{M}^0$, $\mathbf{M}^{-1}$, $\mathbf{M}^{+1}$, $\mathbf{N}^{-1}$ and $\mathbf{N}^{+1}$. When the spatial Fourier wave

$$\bar{v}^n_{i,j;m} = \tilde{v}^n_m e^{I\left[k\left((iB_{1x}+jB_{2x})\cos\theta + \left(iB_{1y}+jB_{2y}\right)\sin\theta\right)\right]}, \tag{25}$$

$m = 1,\ldots,2N^{CV}$, is inserted into (23), the following linear system of equations is obtained:

$$\begin{aligned}\tilde{\mathbf{v}}^{n+1} - \tilde{\mathbf{v}}^{n} + \sigma\mathbf{M}^0\tilde{\mathbf{v}}^{n+1} + \sigma\mathbf{M}^{-1}\tilde{\mathbf{v}}^{n+1}e^{-IK\left(B'_{1x}\cos\theta + B'_{1y}\sin\theta\right)} + \sigma\mathbf{M}^{+1}\tilde{\mathbf{v}}^{n+1}e^{+IK\left(B'_{1x}\cos\theta + B'_{1y}\sin\theta\right)}\\ + \sigma\mathbf{N}^{-1}\tilde{\mathbf{v}}^{n+1}e^{-IK\left(B'_{2x}\cos\theta + B'_{2y}\sin\theta\right)} + \sigma\mathbf{N}^{+1}\tilde{\mathbf{v}}^{n+1}e^{+IK\left(B'_{2x}\cos\theta + B'_{2y}\sin\theta\right)} = 0,\end{aligned} \tag{26}$$

where $K = k\Delta B$ is the non-dimensional wave number. An expression for the amplification matrix $\mathbf{G}_D$, defined by $\tilde{\mathbf{v}}^{n+1} = \mathbf{G}_D\tilde{\mathbf{v}}^n$, can be obtained from Eq. (26):

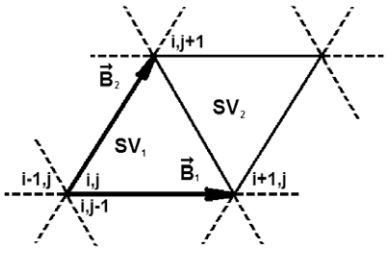

Fig. 2. Generating pattern for the mesh.

$$\mathbf{G}_D = \left[\mathbf{I} + \sigma\mathbf{M}^0 + \sigma\mathbf{M}^{-1}e^{-IK\left(B'_{1x}\cos\theta + B'_{1y}\sin\theta\right)} + \sigma\mathbf{M}^{+1}e^{+IK\left(B'_{1x}\cos\theta + B'_{1y}\sin\theta\right)} + \sigma\mathbf{N}^{-1}e^{-IK\left(B'_{2x}\cos\theta + B'_{2y}\sin\theta\right)} + \sigma\mathbf{N}^{+1}e^{+IK\left(B'_{2x}\cos\theta + B'_{2y}\sin\theta\right)}\right]^{-1}. \tag{27}$$

The matrix $\mathbf{G}_D$ represents the amplification matrix of the direct inversion method which is marked as 'direct + BE' in the remainder of this paper.

The previous analysis may be applied to the LU-SGS + BE scheme to get its amplification matrix. The present LU-SGS algorithm is used to solve a nonlinear system of equations. However, when it is employed to solve a linear problem, it is identical to the classical LU-SGS algorithm proposed in Jameson et al. [22,23]. The main idea of the linear LU-SGS method is to split the matrix $\mathbf{E}$ in Eq. (24) into a diagonal, a strictly lower and a strictly upper matrix,

$$\mathbf{E} = \mathbf{D} + \mathbf{L} + \mathbf{U} \tag{28}$$

and solve the linear system with forward and backward Gauss–Seidel sweeps:

$$(\mathbf{D} + \mathbf{L})\tilde{\mathbf{v}}^{h+1/2} + \mathbf{U}\tilde{\mathbf{v}}^{h} = \tilde{\mathbf{v}}^{n}, \tag{29a}$$

$$(\mathbf{D} + \mathbf{U})\tilde{\mathbf{v}}^{h+1} + \mathbf{L}\tilde{\mathbf{v}}^{h+1/2} = \tilde{\mathbf{v}}^{n}, \tag{29b}$$

where $h = 0, 1, 2, 3, \ldots$ is the actual SGS sweep index. The first equation, with solution $\tilde{\mathbf{v}}^{h+1/2}$, corresponds to the forward sweep and the second one, with solution $\tilde{\mathbf{v}}^{h+1}$ represents the backward sweep. Note that $\tilde{\mathbf{v}}^{h=0} = \tilde{\mathbf{v}}^{n}$. To derive the amplification matrix for the LU-SGS method, the matrix $\mathbf{M}^0$ has to be split in the following form:

$$\mathbf{M}^0 = \mathbf{M}^0_{1,1} + \mathbf{M}^0_{1,2} + \mathbf{M}^0_{2,1} + \mathbf{M}^0_{2,2}, \tag{30}$$

where $\mathbf{M}^0_{1,1}$ and $\mathbf{M}^0_{2,2}$ represent, respectively the contribution to the residual of the first and second cell of the generating pattern to themselves, while $\mathbf{M}^0_{1,2}$ and $\mathbf{M}^0_{2,1}$ represent the cross contributions of both cells of the generating pattern. After substituting Eq. (30) into Eq. (26), the equation of the amplification matrix for the first forward sweep becomes

$$\begin{aligned}
&\tilde{\mathbf{v}}^{1/2} - \tilde{\mathbf{v}}^{n} + \sigma\mathbf{M}^0_{1,1}\tilde{\mathbf{v}}^{1/2} + \sigma\mathbf{M}^0_{1,2}\tilde{\mathbf{v}}^{n} + \sigma\mathbf{M}^0_{2,1}\tilde{\mathbf{v}}^{1/2} + \sigma\mathbf{M}^0_{2,2}\tilde{\mathbf{v}}^{1/2} + \sigma\mathbf{M}^{-1}\tilde{\mathbf{v}}^{1/2}e^{-IK\left(B'_{1x}\cos\theta + B'_{1y}\sin\theta\right)} \\
&\quad + \sigma\mathbf{M}^{+1}\tilde{\mathbf{v}}^{n}e^{+IK\left(B'_{1x}\cos\theta + B'_{1y}\sin\theta\right)} + \sigma\mathbf{N}^{-1}\tilde{\mathbf{v}}^{1/2}e^{-IK\left(B'_{2x}\cos\theta + B'_{2y}\sin\theta\right)} + \sigma\mathbf{N}^{+1}\tilde{\mathbf{v}}^{n}e^{+IK\left(B'_{2x}\cos\theta + B'_{2y}\sin\theta\right)} \\
&\quad = 0,
\end{aligned} \tag{31}$$

from which the amplification matrix of the first forward sweep (32) is found.

$$\begin{aligned}
\mathbf{G}_{f,1} = &\left[\mathbf{I} + \sigma\mathbf{M}^0_{1,1} + \sigma\mathbf{M}^0_{2,1} + \sigma\mathbf{M}^0_{2,2} + \sigma\mathbf{M}^{-1}e^{-IK\left(B'_{1x}\cos\theta + B'_{1y}\sin\theta\right)} + \sigma\mathbf{N}^{-1}e^{-IK\left(B'_{2x}\cos\theta + B'_{2y}\sin\theta\right)}\right]^{-1} \\
&\times \left[\mathbf{I} - \sigma\mathbf{M}^0_{1,2} - \sigma\mathbf{M}^{+1}e^{+IK\left(B'_{1x}\cos\theta + B'_{1y}\sin\theta\right)} - \sigma\mathbf{N}^{+1}e^{+IK\left(B'_{2x}\cos\theta + B'_{2y}\sin\theta\right)}\right].
\end{aligned} \tag{32}$$

For the first backward sweep, in accordance with Eq. (29b), we get

$$\begin{aligned}
&\tilde{\mathbf{v}}^{1} - \tilde{\mathbf{v}}^{n} + \sigma\mathbf{M}^0_{1,1}\tilde{\mathbf{v}}^{1} + \sigma\mathbf{M}^0_{1,2}\tilde{\mathbf{v}}^{1} + \sigma\mathbf{M}^0_{2,1}\tilde{\mathbf{v}}^{1/2} + \sigma\mathbf{M}^0_{2,2}\tilde{\mathbf{v}}^{1} + \sigma\mathbf{M}^{-1}\tilde{\mathbf{v}}^{1/2}e^{-IK\left(B'_{1x}\cos\theta + B'_{1y}\sin\theta\right)} \\
&\quad + \sigma\mathbf{M}^{+1}\tilde{\mathbf{v}}^{1}e^{+IK\left(B'_{1x}\cos\theta + B'_{1y}\sin\theta\right)} + \sigma\mathbf{N}^{-1}\tilde{\mathbf{v}}^{1/2}e^{-IK\left(B'_{2x}\cos\theta + B'_{2y}\sin\theta\right)} + \sigma\mathbf{N}^{+1}\tilde{\mathbf{v}}^{1}e^{+IK\left(B'_{2x}\cos\theta + B'_{2y}\sin\theta\right)} = 0.
\end{aligned} \tag{33}$$

Hence, the amplification matrix of the first SGS sweep is given by

$$\begin{aligned}
\mathbf{G}_{SGS,1} = &\left[\mathbf{I} + \sigma\mathbf{M}^0_{1,1} + \sigma\mathbf{M}^0_{1,2} + \sigma\mathbf{M}^0_{2,2} + \sigma\mathbf{M}^{+1}e^{+IK\left(B'_{1x}\cos\theta + B'_{1y}\sin\theta\right)} + \sigma\mathbf{N}^{+1}e^{+IK\left(B'_{2x}\cos\theta + B'_{2y}\sin\theta\right)}\right]^{-1} \\
&\times \left[\mathbf{I} - \sigma\mathbf{G}_{f,1}\mathbf{M}^0_{2,1} - \sigma\mathbf{M}^{-1}\mathbf{G}_{f,1}e^{-IK\left(B'_{1x}\cos\theta + B'_{1y}\sin\theta\right)} - \sigma\mathbf{N}^{-1}\mathbf{G}_{f,1}e^{-IK\left(B'_{2x}\cos\theta + B'_{2y}\sin\theta\right)}\right].
\end{aligned} \tag{34}$$

From the amplification matrix $\mathbf{G}_{SGS,1}$, the amplification matrix of hth SGS sweep may be computed using the following two-step recursive procedure:

- Compute the amplification matrix of the hth forward sweep

$$\begin{aligned}
\mathbf{G}_{f,h} = &\left[\mathbf{I} + \sigma\mathbf{M}^0_{1,1} + \sigma\mathbf{M}^0_{2,1} + \sigma\mathbf{M}^0_{2,2} + \sigma\mathbf{M}^{-1}e^{-IK\left(B'_{1x}\cos\theta + B'_{1y}\sin\theta\right)} + \sigma\mathbf{N}^{-1}e^{-IK\left(B'_{2x}\cos\theta + B'_{2y}\sin\theta\right)}\right]^{-1} \\
&\times \left[\mathbf{I} - \sigma\mathbf{G}_{SGS,h-1}\mathbf{M}^0_{1,2} - \sigma\mathbf{M}^{+1}\mathbf{G}_{SGS,h-1}e^{+IK\left(B'_{1x}\cos\theta + B'_{1y}\sin\theta\right)} - \sigma\mathbf{N}^{+1}\mathbf{G}_{SGS,h-1}e^{+IK\left(B'_{2x}\cos\theta + B'_{2y}\sin\theta\right)}\right].
\end{aligned} \tag{35}$$

- Compute the amplification matrix of the hth SGS sweep

$$\begin{aligned}
\mathbf{G}_{SGS,h} = &\left[\mathbf{I} + \sigma\mathbf{M}^0_{1,1} + \sigma\mathbf{M}^0_{1,2} + \sigma\mathbf{M}^0_{2,2} + \sigma\mathbf{M}^{+1}e^{+IK\left(B'_{1x}\cos\theta + B'_{1y}\sin\theta\right)} + \sigma\mathbf{N}^{+1}e^{+IK\left(B'_{2x}\cos\theta + B'_{2y}\sin\theta\right)}\right]^{-1} \\
&\times \left[\mathbf{I} - \sigma\mathbf{M}^0_{2,1}\mathbf{G}_{f,h} - \sigma\mathbf{M}^{-1}\mathbf{G}_{f,h}e^{-IK\left(B'_{1x}\cos\theta + B'_{1y}\sin\theta\right)} - \sigma\mathbf{N}^{-1}\mathbf{G}_{f,h}e^{-IK\left(B'_{2x}\cos\theta + B'_{2y}\sin\theta\right)}\right].
\end{aligned} \tag{36}$$

Let $\lambda_m (m = 1, \ldots, 2N^{CV})$ be an eigenvalue of the general amplification matrix $\mathbf{G} = \mathbf{G}(K, \theta, \psi)$ and $\lambda = \lambda(\mathbf{G}(K, \theta, \psi))$ represent the eigenvalue spectrum of $\mathbf{G}$. Then $g = g(K, \theta, \psi) \equiv max[|\lambda(\mathbf{G})|]$ is the amplification factor for a given (K, θ, ψ). In order for the scheme to be stable, $g \leqslant 1$ should be satisfied i.e. $\lambda(\mathbf{G})$ lies inside the unit circle of the complex plane (stability boundary) for all K, θ and ψ. The range of K is one period of the Eq. (26) and it will be marked P in the remainder of this paper. For a fixed shape of the generating pattern, P is a function of θ, i.e. $P = P(\theta)$. The expression from which P can be computed is obtained by substituting $\mathbf{B}_1', \mathbf{B}_2'$ and θ in the exponential terms of Eq. (26) and using the Euler's formula, which gives a relation between the trigonometric functions and the complex numbers. Following this reasoning, a trigonometric function f, which has exactly the same period as Eq. (26) is obtained. In general, it is not possible to find a closed formulation for $P = P(\theta)$. Therefore, the period P is computed taking the inverse fast Fourier transformation of the function f.

If the scheme is used as a smoother for multigrid, then it must have good damping of high-frequency error components, i.e. it should cluster the eigenvalues of the amplification matrix corresponding to the high-frequency modes towards the origin of the complex plane. Therefore, for high-frequency modes $g \ll 1$ for all θ and ψ should be satisfied. In addition, we desire that the CFL number is sufficiently large to produce significant reduction (if not elimination) of the convergence slow-down effects that are associated with high-aspect ratio mesh cells. A large CFL number also facilitates the expulsion of error components. At the same time the capability for large CFL numbers must not compromise the high-frequency damping properties of the scheme.

In the following section, the damping properties of the LU-SGS + BE method for the second-order SV scheme will be analyzed to provide the value of the number of symmetric Gauss–Seidel sweeps for carrying out the numerical tests of Section 8. However, since the performance of the direct inversion method is better than that of any approximate method, the direct inversion method is examined as a baseline for comparison with the LU-SGS algorithm.

In the present analysis, an upwind Riemann flux ($\varphi = 1$ in Eq. (21)) is employed and the direction of the wave propagation velocity ψ is set to $-\frac{\pi}{6} (a_x > 0, a_y < 0)$. A negative y velocity component is chosen to avoid having the sweep directions of the

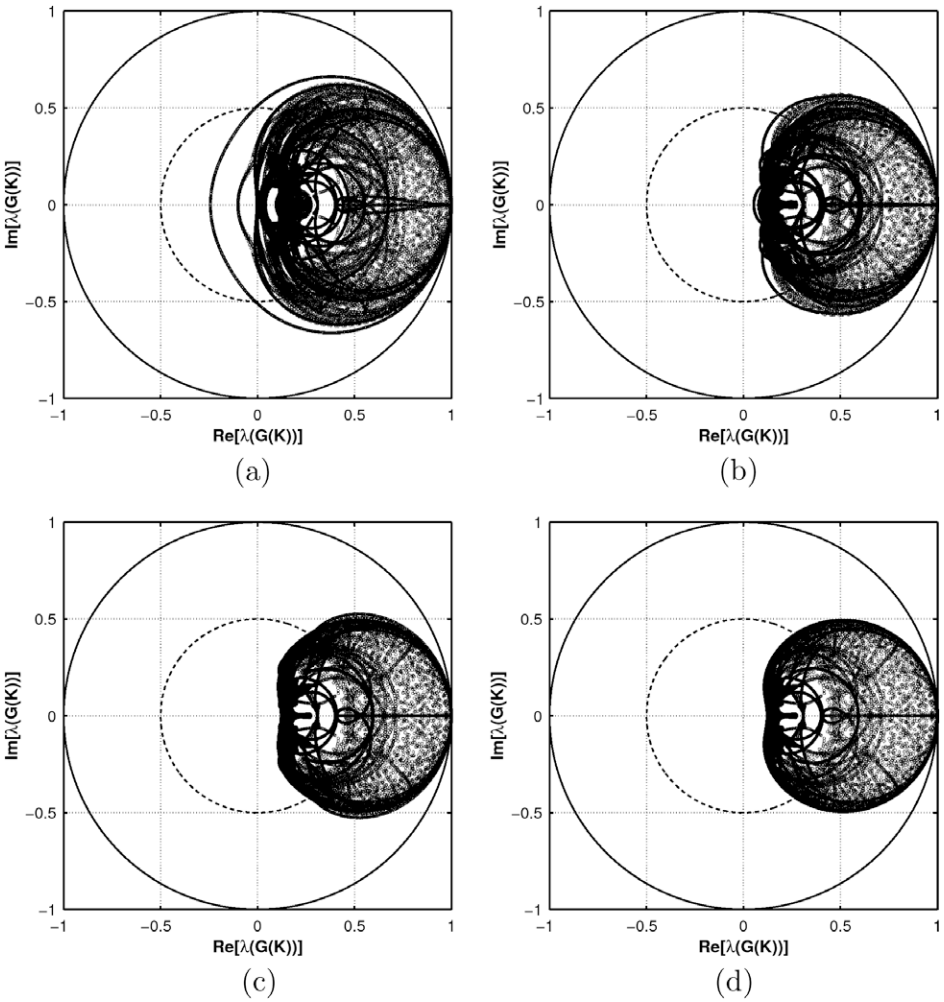

Fig. 3. Effect of the SGS sweeps on the eigenvalue spectrum of the LU-SGS + BE scheme applied to 2D linear convection equation. SV2 scheme, upwind Riemann flux, $\psi \in [0, 2\pi]$, $\theta \in [0, 2\pi]$, $K \in [0, P(\theta)]$, $AR = 1$, CFL = 1. (a) 1 SGS sweep, (b) 2 SGS sweeps, (c) 3 SGS sweeps, and (d) direct + BE method.

LU-SGS method aligned with the flow direction. In fact, if the flow direction corresponds to the sweep directions, the LU-SGS becomes a direct solver, e.g. in case of a purely upwind scheme. The smoothing properties of the direct method and the LU-SGS + BE method are shown for three values of the solution orientation θ, i.e $-\frac{\pi}{6}, 0$ and $\frac{\pi}{3}$ and two meshes with respectively an aspect ratio of one and hundred. The latter mesh accounts for the effects of the geometrical stiffness imposed by the Navier–Stokes grids where high-aspect ratios occur near walls.

7. Second-order SV scheme

First, consider a mesh built from equilateral triangles. Such a mesh is obtained with the following choice for the dimensionless vectors $\mathbf{B}'_1$ and $\mathbf{B}'_2$,

$$\mathbf{B}'_1 = \begin{pmatrix} 1 \\ 0 \end{pmatrix} \quad \mathbf{B}'_2 = \begin{pmatrix} \frac{1}{2} \\ \frac{\sqrt{3}}{2} \end{pmatrix} \tag{37}$$

and leads to a mesh with isotropic cells, i.e. the aspect ratio, $AR = \frac{|\mathbf{B}'_1|}{|\mathbf{B}'_2|} = 1$. Fig. 3 shows the eigenvalue spectrum of the amplification matrix of the LU-SGS + BE method and the direct + BE method on the equilateral triangle mesh, for CFL = 1, varying the direction ψ of the wave propagation velocity **a**, the wave number K, and the solution orientation defined by the angle θ. For the LU-SGS + BE one, two and three SGS sweeps are used. It is seen that the SV2 scheme with the LU-SGS + BE method is stable for all K, θ and ψ. Fig. 3 shows that with an increasing number of SGS sweeps, the eigenvalue spectrum of the LU-SGS + BE method approaches that of the direct + BE method.

Our aim is to plot the amplification factor g as a function of the wave number K. Hence, in the following paragraphs we are going to present first the analysis of the smoothing properties done for the direct + BE solver and to describe the methodology used to plot correctly the amplification factor g. First, consider a solution with an orientation $\theta = \psi = -\frac{\pi}{6}$. For this choice, Eq. (26) is periodic in K with a period equal to $\frac{4}{\sqrt{3}\pi}$. However, Eq. (26) has N^{CV} eigenvalues for each K and, as was pointed out

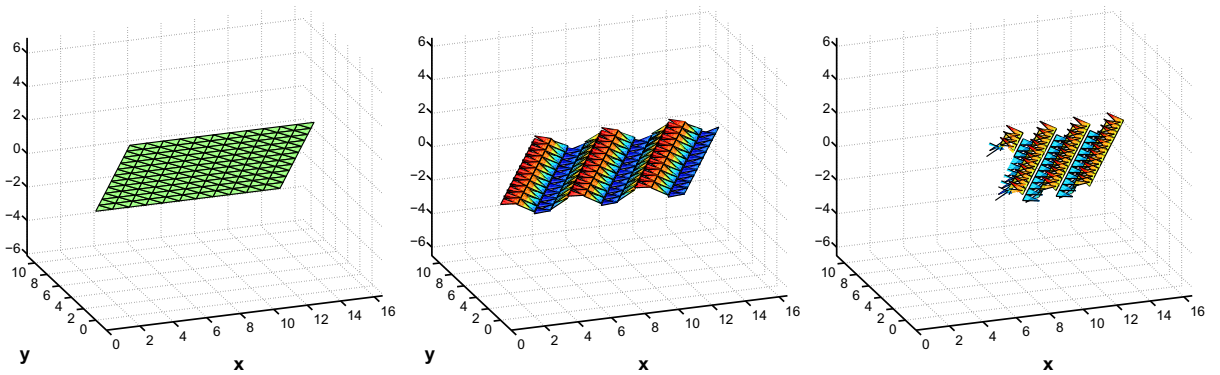

in [15,31], each eigenvalues corresponds to a wave number $K + z\frac{4}{\sqrt{3}}\pi$, with z an integer number. Consequently, to get the correct damping properties of the solver, each mode should be shifted by a multiple of $\frac{4}{\sqrt{3}}\pi$ along the wave number axis. The actual wave number $K + z\frac{4}{\sqrt{3}}\pi$ to which an eigenvalue $\lambda_m (m = 1, \ldots, 2N^{CV})$ corresponds has to be determined by examining the spatial shape of the eigenmode, defined by the eigenvector $\hat{\mathbf{v}}_m$

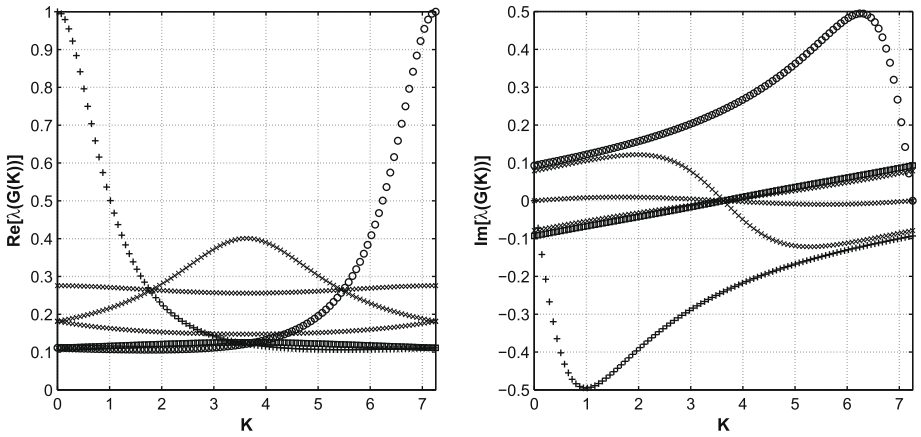

Fig. 5. Direct inversion method applied to 2D convection equation. SV2 method, upwind Riemann flux, $\theta = \psi = -\frac{\pi}{6}$, $AR = 1$, CFL = 1. Real and imaginary part of the eigenvalue spectrum of the amplification matrix.

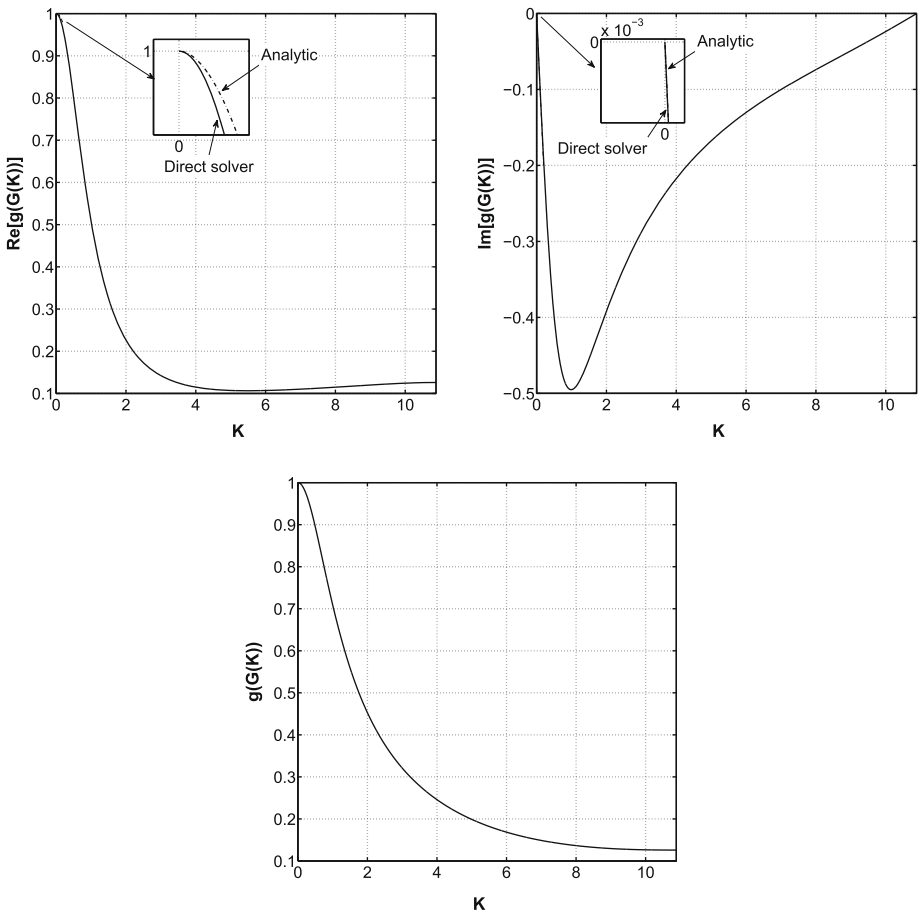

Fig. 6. Direct inversion method applied to 2D convection equation. SV2 method, upwind Riemann flux, $\theta = \psi = -\frac{\pi}{6}$, $AR = 1$, CFL = 1. Real part, imaginary part and absolute value of the amplitude of the amplification matrix.

$$\hat{\mathbf{v}}_m e^{I\left[K\left(\left(iB'_{1x}+jB'_{2x}\right)\cos\theta+\left(iB'_{1y}+jB'_{2y}\right)\sin\theta\right)\right]} \tag{38}$$

and whose shape are shown in Fig. 4 for $K = l\frac{\pi}{\sqrt{3}} l = 0,\ldots,5$.

In Fig. 5 the eigenvalue spectrum $\lambda(\mathbf{G}_D)$ is plotted as a function of the wave number K, for $\psi = \theta = -\frac{\pi}{6}$, for an upwind Riemann flux and CFL = 1. For small wave numbers K, the shape of the eigenmodes reveals the correct wave number to which an eigenvalue corresponds. In fact, in Fig. 5 three curves can readily be selected by examining the spatial shape of the eigenvector (see Fig. 4), namely the curves marked by the plus (+), the square (□) and the circle (○) signs. The other curves, marked by the (×) sign, corresponds to eigenvalues which belong to a higher wave number range of K compared with the eigenvalues of three selected curves. From Fig. 4 it is clear that the amplitude of the discontinuities in the numerical solution at the cell interfaces grow with increasing wave number K which makes difficult the analysis of the eigenvectors and the selection of the actual wave number $K + z\frac{4}{\sqrt{3}}\pi$ to which an eigenvalue corresponds. Therefore, for a high-wave number, the effort of associating each eigenvalue with the corresponding wave number K has not been performed. However, the eigenvalues which correspond to a high-wave number K, thus the eigenvalues marked by the sign (×), are well damped as it is seen again from Fig. 5. Therefore, shifting these curves in the appropriate way, leads to plots as in Fig. 6. Because of the symmetry $(Re[\lambda(\mathbf{G}(K))] = Re[\lambda(\mathbf{G}(-K))]$ and $Im[\lambda(\mathbf{G}(K))] = -Im[\lambda(\mathbf{G}(-K))])$, the curves are only shown for positive wave numbers $K \in [0, \frac{3}{2}P]$.

In this case, the direct solver is a physically accurate scheme and its amplification factor should follow closely the exact amplification factor relation given by Eq. (39),

$$G_{exact} = \frac{v(t+\delta t)}{v(t)} = e^{-Ika\Delta t}, \tag{39}$$

which for wave numbers K close to zero ($K\Delta t \ll 1$) can be approximated in a Taylor series by

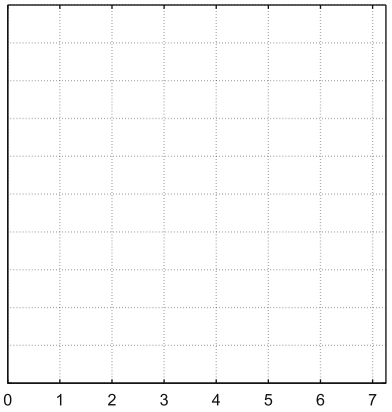

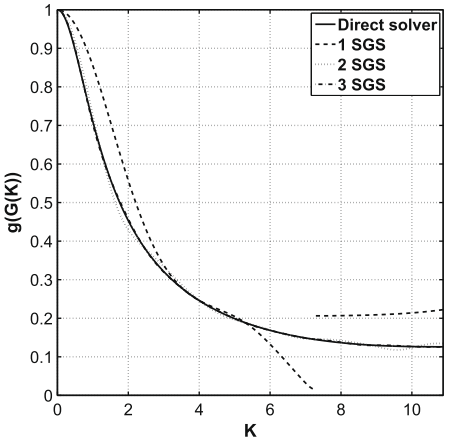

Fig. 8. Effect of the SGS sweeps on the amplification factor of the LU-SGS + BE scheme applied to 2D linear convection equation. SV2 scheme, upwind Riemann flux, $\theta = \psi = -\frac{\pi}{6}$, $K \in [0, \frac{3}{2}P]$, $AR = 1$, CFL = 1.

$$G_{exact} \approx 1 - IKa\Delta t - \frac{K^2 a^2 \Delta t^2}{2} + o(K^3 \Delta t^3). \tag{40}$$

In the first two plots of Fig. 6, the real and the imaginary part of the amplification factor of the direct solver for $K\Delta t$ close to zero are plotted along with their counterparts in Eq. (40). It is seen that the direct + BE method follow closely the theoretical results for $K\Delta t \ll 1$. In the last plot of Fig. 6 the amplification factor g of the direct + BE inversion method is plotted as a function of the wave number $K \in [0, \frac{3}{2}P]$, for $\theta = \psi = -\frac{\pi}{6}$. It is seen that the direct + BE solver has good damping properties for high-frequency solution components.

The procedure described above may be applied to the amplification matrix of the LU-SGS + BE scheme. In Fig. 7 the eigenvalue spectrum $\lambda(\mathbf{G}_D)$ is plotted as a function of the wave number K, for $\psi = \theta = -\frac{\pi}{6}$ with an upwind Riemann flux, for CFL = 1 and one SGS sweep. In this figure, three curves marked with the plus sign (+), the square (□) and the circle (○) are shown (cf. Fig. 5). Shifting these curves in the appropriate, way the amplification factor curve of Fig. 8 for $K \in [0, \frac{3}{2}P]$ is found. In the same plot, the amplification factor for two and three sweeps is also shown. It is seen that the discontinuity, obtained with one SGS sweep, disappears when two SGS sweeps are employed. For three SGS sweeps the amplification factor of the LU-SGS + BE method is indistinguishable from that of the direct + BE inversion method. This explains why for the analysis of a mesh with $AR = 1$ and CFL = 1, a maximum number of three SGS sweeps was used.

Consider the same equilateral triangle mesh but with a CFL number of 10^6. The eigenvalue spectrum of the amplification matrix of the direct + BE and the LU-SGS + BE methods for this case is plotted in Fig. 9, varying again the direction ψ of wave propagation velocity **a**, the wave number K and the angle θ. For the LU-SGS + BE method, one, ten and one hundred SGS sweeps are employed. It is seen that for CFL = 10^6, the LU-SGS + BE method is still stable for all K, θ and ψ. However, using

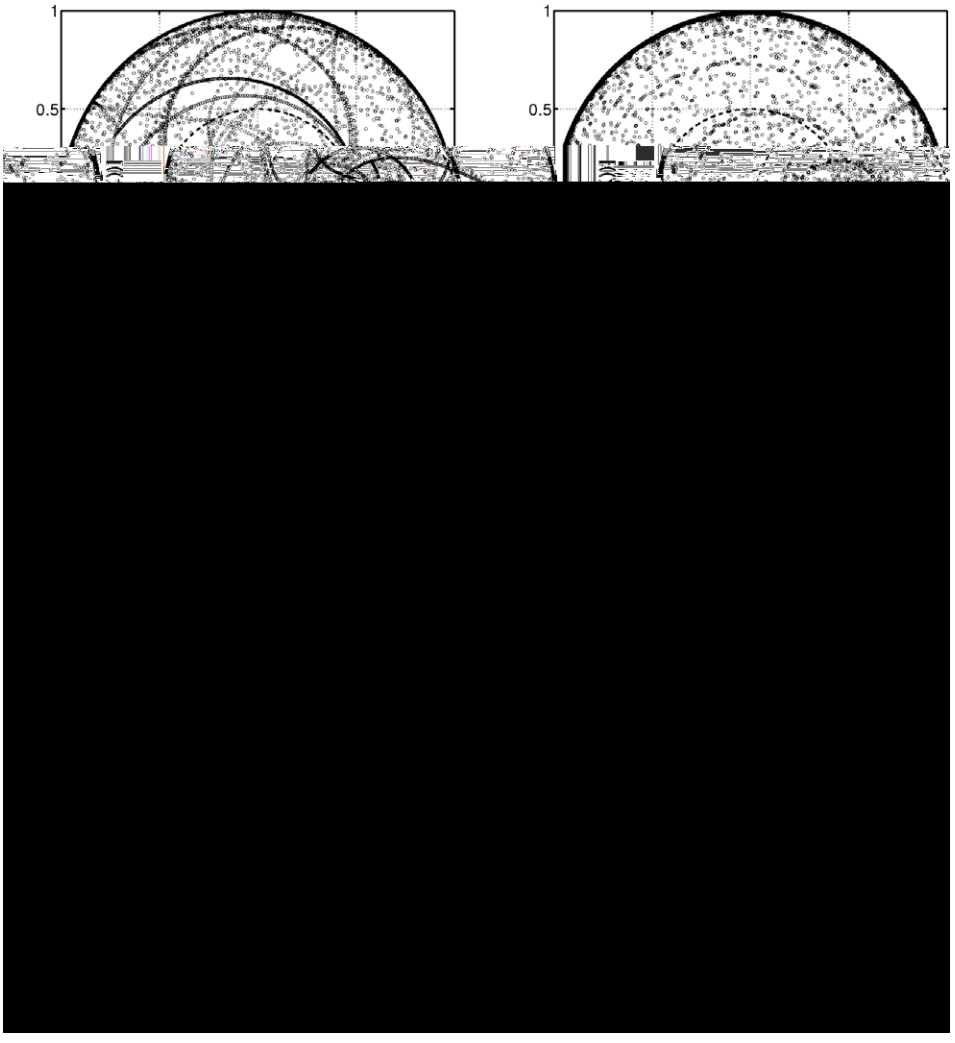

Fig. 9. Effect of the SGS sweeps on the eigenvalue spectrum of the LU-SGS + BE scheme applied to 2D linear convection equation. SV2 scheme, upwind Riemann flux, $\psi \in [0, 2\pi]$, $\theta \in [0, 2\pi]$, $K \in [0, P(\theta)]$, $AR = 1$, CFL $= 10^6$. (a) 1 SGS sweep, (b) 10 SGS sweeps, (c) 100 SGS sweeps, and (d) direct + BE method.

too few SGS sweeps (1–3 sweeps), the scheme exhibits poor damping behavior for some values of the angle θ and a range of frequencies K. In Figs. 10–12 the amplification factor for $\theta = -\frac{\pi}{6}, \theta = 0$ and $\theta = \frac{\pi}{3}$ are shown for CFL = 10^6. Fig. 11 shows that for $\theta = 0$ the amplification factor exhibits a discontinuity for a wave number equal to half the period of Eq. (26), i.e. for $K = 2\pi$. In fact, the amplification factor starts from one for $K = 0$, and it decreases very fast to zero for $K > 0$. However, when $K = 2\pi$, it jumps to a value which is again close to (0.9–1) and then it rapidly decreases again for high-wave numbers. Notice, that the discontinuity occurs at a low-frequency wave number i.e. at a frequency which is $\frac{1}{6}$ of the whole wave number covered by the spatial scheme. By increasing the number of SGS sweeps, the amplitude of the discontinuity decreases but for one hundred SGS sweeps the curve is still discontinuous and it differs from that of the direct + BE method. Figs. 10 and 12 show that for $\theta = -\frac{\pi}{6}$ and $\theta = \frac{\pi}{3}$ the high-frequency error components are well damped and they do not exhibit jumps as for $\theta = 0$. Moreover, for these two values of θ, the amplification factor also shows a discontinuity which disappears when five or more SGS sweeps are employed.

Now, to study the damping properties of the LU-SGS + BE scheme when the geometrical stiffness imposed by the Navier–Stokes grids occur near walls, consider a mesh obtained for the following choice of the dimensionless vectors $\mathbf{B}'_1$ and $\mathbf{B}'_2$,

$$\mathbf{B}'_1 = \begin{pmatrix} 1 \\ 0 \end{pmatrix} \quad \mathbf{B}'_2 = \begin{pmatrix} 0 \\ \frac{1}{100} \end{pmatrix}. \tag{41}$$

This mesh has anisotropic cells with $AR = 100$. The eigenvalue spectrum of the amplification matrix of the LU-SGS+BE and the direct + BE methods is plotted in Fig. 13 for CFL = 10^6, varying again the direction ψ of wave propagation velocity $\mathbf{a}$, the wave number K and angle θ. One, ten and hundred SGS sweeps are employed. The plots show that the LU-SGS + BE method is still stable for all K, θ and ψ but when only a few SGS sweeps are employed (1–3 sweeps), it exhibits a poor damping behavior for some values of the angle θ and a range of frequencies K.

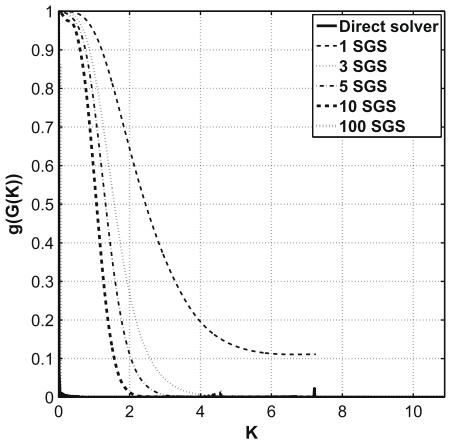

Fig. 10. Effect of the SGS sweeps on the amplification factor of the LU-SGS + BE scheme applied to 2D linear convection equation. SV2 scheme, upwind Riemann flux, $\theta = \psi = -\frac{\pi}{6},\ K \in [0, \frac{3}{2}P],\ AR = 1$, CFL = 10^6.

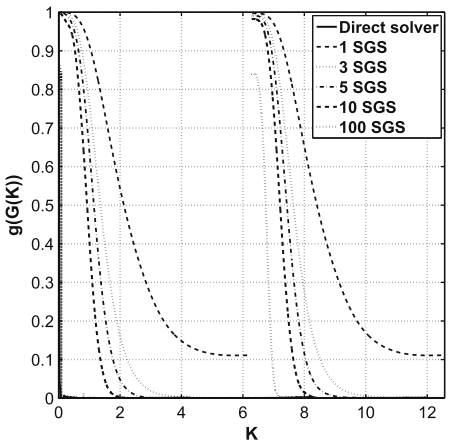

Fig. 11. Effect of the SGS sweeps on the amplification factor of the LU-SGS + BE scheme applied to 2D linear convection equation. SV2 scheme, upwind Riemann flux, $\psi = -\frac{\pi}{6},\ \theta = 0,\ K \in [0, P],\ AR = 1$, CFL = 10^6.

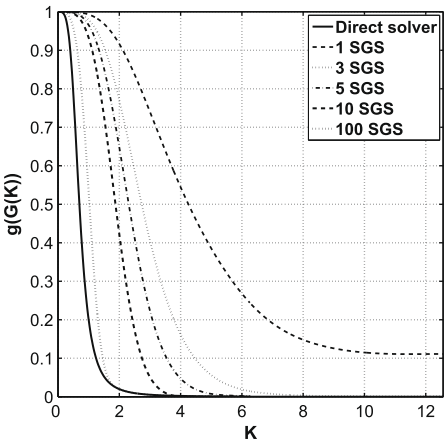

Fig. 12. Effect of the SGS sweeps on the amplification factor of the LU-SGS + BE scheme applied to 2D linear convection equation. SV2 scheme, upwind Riemann flux, $\psi = -\frac{\pi}{6},\ \theta = \frac{\pi}{3},\ K \in [0, \frac{1}{2}P],\ AR = 1$, CFL = 10^6.

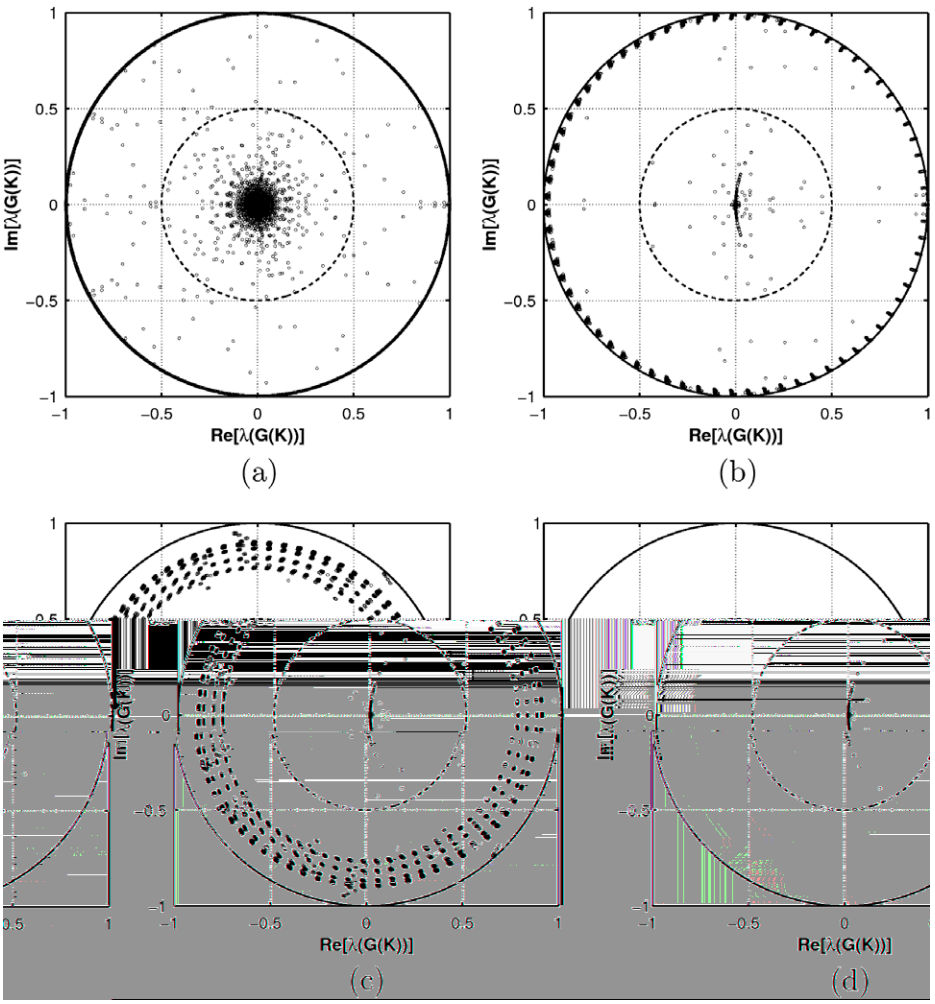

Fig. 13. Effect of the SGS sweeps on the eigenvalue spectrum of the LU-SGS + BE scheme applied to 2D linear convection equation. SV2 scheme, upwind Riemann flux, $\psi \in [0, 2\pi],\ \theta \in [0, 2\pi],\ K \in [0, P(\theta)],\ AR = 100,\ \text{CFL} = 10^6$. (a) 1 SGS sweep, (b) 10 SGS sweeps, (c) 100 SGS sweeps, and (d) direct + BE method.

As for a mesh with $AR = 1$, in Figs. 14–16 the amplification factor of both direct and LU-SGS methods are plotted as a function of the wave number K, for $\theta = -\frac{\pi}{6}$, $\theta = 0$ and $\theta = \frac{\pi}{3}$. In these cases,the period P of the Eq. (26) for the three values of the solution orientation is respectively, $\frac{2\pi}{\sin\frac{\pi}{6}}, 2\pi$ and $\frac{2\pi}{\sin\frac{\pi}{3}}$.

It is seen that, when few SGS sweeps (3–5) are employed, the damping properties of the LU-SGS + BE solver for $\theta = -\frac{\pi}{6}$ and $\theta = \frac{\pi}{3}$ are similar to that of the direct + BE method, Figs. 14 and 16. For $\theta = 0$ (Fig. 15) the behavior is different. In fact, the low-frequency error components are not damped at all and the amplification factor for a wave number range $[0, \pi)$ is close to one. However, for $K > \pi$ it jumps to a value close to zero and the high-frequency error components are still well damped.

7.1. Remarks

The analysis has demonstrated that the LU-SGS + BE scheme is always stable for any choice of the convective velocity direction ψ and the solution orientation θ for the second-order spectral volume scheme. Furthermore, the analysis has shown that the smoothing properties of the implicit solver depend strongly on the orientation of the solution and on the CFL number. It is seen that increasing the number of the SGS sweeps the damping behavior of the lower–upper symmetric Gauss–Seidel algorithm with the backward Euler scheme gets closer to the damping properties of a direct solver + BE scheme.

The analysis was performed for a CFL of 10^6 and on two meshes with an aspect ratio of one and hundred, respectively. The latter mesh allows to take into account the effects of the geometrical stiffness imposed by the Navier–Stokes grids where high-aspect ratios occur near walls. It was shown that for both meshes 5 SGS sweeps are in general sufficient to get a good damping of the high-frequency error components. Moreover, it has been shown that the amplification factor may have a discontinuity for a certain wave number. This depends on the direction of the harmonic wave solution and the number of SGS sweeps. Nevertheless, the high-frequency error components are always well damped. Besides, for a specific direction of the

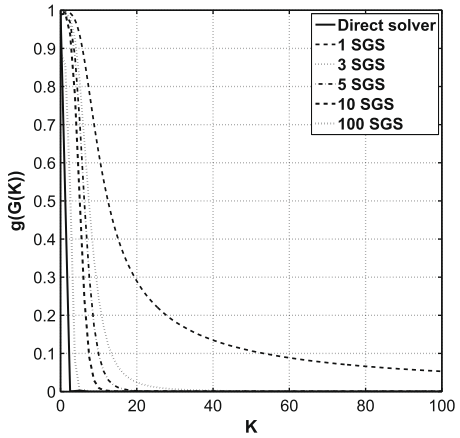

Fig. 14. Effect of the SGS sweeps on the amplification factor of the LU-SGS + BE scheme applied to 2D linear convection equation. SV2 scheme, upwind Riemann flux, $\theta = \psi = -\frac{\pi}{6}$, $K \in [0, 100]$, $AR = 100$, CFL $= 10^6$.

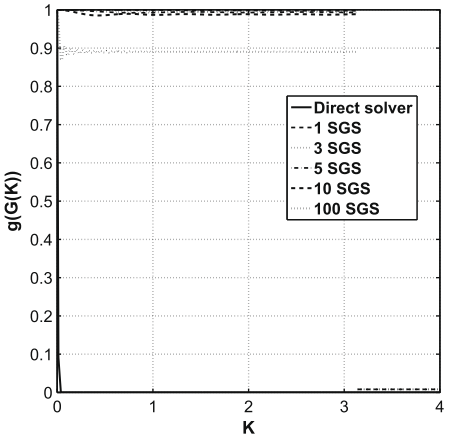

Fig. 15. Effect of the SGS sweeps on the amplification factor of the LU-SGS + BE scheme applied to 2D linear convection equation. SV2 scheme, upwind Riemann flux, $\psi = -\frac{\pi}{6}$, $\theta = 0$, $K \in [0, P]$, $AR = 100$.CFL $= 10^6$.

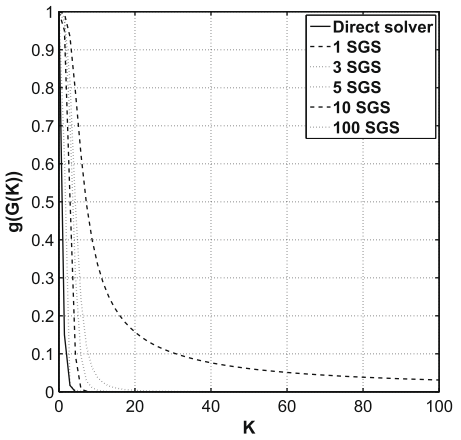

Fig. 16. Effect of the SGS sweeps on the amplification factor of the LU-SGS + BE scheme applied to 2D linear convection equation. SV2 scheme, upwind Riemann flux, $\psi = -\frac{\pi}{6},\ \theta = \frac{\pi}{3},\ K \in [0, 100],\ AR = 100,\ \mathrm{CFL} = 10^6$.

harmonic wave solution ($\theta = 0$) of the 2D linear convection equation, the implicit iterative scheme shows an amplification factor which is close to 1 for a wave number range equal to half of the period of Eq. (26). For wave numbers higher than half of the period the amplification factor is close to zero.

8. Numerical results

The LU-SGS + BE scheme was used to compute the solution of a steady, laminar flow over a cylinder and an airfoil. The solution was calculated with the SV2 method and the *p*-multigrid algorithm with two-level *V*-cycles. The order was restricted to 2 because of the curved boundaries. A first-order interpolation was used for the boundary shape, but high-order schemes would require a more accurate interpolation, especially on the relatively coarse grids that are being used in combination with high-order polynomial representations of the solution [13].

The results are compared with those obtained with optimized E-RK smoothers presented in Section 4 and for the NACA0012 test case also with those obtained with the code of Swanson et al. [21].

The linear system (17) is solved with multiple cell-wise symmetric forward and backward sweeps with a prescribed tolerance of 10^{-6} on the change of the L_2 norm of the solution variation $\widetilde{\Delta\mathbf{W}}_c^{(k+1)}$ and/or a maximum number of 6 SGS sweeps. For all the calculations, a maximum CFL number of 10^6 is employed. The former choices allow strong damping of the high-frequency error components and gives good properties in terms of CPU-time and convergence rate for the steady state computations. From the Von Neumann analysis of the 2D linear advection equation it was found that a maximum number of 5–6 SGS sweeps are in general sufficient to get good damping of the high-frequency error components for a CFL number of 10^6. For the present test cases, if a CFL number larger than 10^6 is used, the convergence rate and the CPU-time of the LU-SGS + BE scheme do not improve. Therefore, increasing the CFL number above 10^6 does not yield any speed-up of the implicit LU-SGS + BE scheme.

Unless indicated otherwise, the calculations were started with the lower order discretization (full *p*-multigrid algorithm). The residuals are normalized by the corresponding residuals of the first iteration. The grids were created using the Gmsh software [33] which allows a second-order ($p = 2$) polynomial approximation of the curved boundary elements. Although, the cells' numbering potentially has an important influence on the convergence of the scheme due to the nature of the implicit LU-SGS (see [32]), in the present work, the order of the cells in the cell index list is not reordered with any criteria or algorithm and it corresponds to the Gmsh numbering. In the Gmsh software, the element numbers are assigned by looping over geometrical entities of increasing dimensions (points, then curves, then surfaces, then volumes) and numbering the cells "as they come" in each entity [33]. The calculations were performed on a Linux workstation with an Intel T2500 Core Duo (2.0 GHz) processor.

8.1. Laminar flow over a cylinder

The compressible laminar flow simulation over a cylinder was conducted at free-stream Mach number of 0.15, Reynolds number based on the cylinder diameter of 40 and Prandtl number of 0.72. First, a grid with 3744 triangular cells with a maximum AR (AR_{max}) of 2 was used. In the first part of the Table 2 we list the CFL numbers for the E-RK and the LU-SGS + BE schemes. For the E-RK scheme two values for the CFL number are indicated; the first one is the convective CFL number σ_{conv} while the second one is the viscous CFL number σ_{visc}. From these two CFL values two local time-steps are computed:

Table 2
CFL number for the two-level *V*-cycles for the subsonic laminar cylinder flow. Unstructured grids with 3744 cells, $AR_{max} = 2$, and 5440 cells, $AR_{max} = 162$.

Scheme	$AR_{max} = 2$		$AR_{max} = 162$	
	SV1	SV2	SV1	SV2
Opt. explicit R–K	7, 0.5	4, 0.3	1.5, 0.01	0.35, 0.005
LU-SGS + BE	10^n	10^n	10^n	10^n

$$\Delta t_{conv} = \frac{\sigma_{conv} V}{\sum_{j=1}^{N^{faces}} \mathbf{a}_j \cdot \mathbf{S}_j + c_j |\mathbf{S}_j|} \tag{42}$$

and

$$\Delta t_{visc} = \frac{\sigma_{visc} V^2}{\sum_{j=1}^{N^{faces}} \nu |\mathbf{S}_j|^2}, \tag{43}$$

where N^{faces}, $\mathbf{S}_j$, $\mathbf{a}_j$, c_j and ν, represent respectively, the number of faces of the spectral volume SV, the jth oriented surface, the local convective velocity, the local speed of sound and the kinematic viscosity. To compute the cell's solution at the next time-level, the minimum value between Δt_{conv} and Δt_{visc} is selected.

For the LU-SGS + BE scheme both maximum convective and viscous CFL numbers were set to 10^6 for each p-multigrid level. In Fig. 17, the convergence histories of the continuity equation of the E-RK scheme and LU-SGS + BE scheme are compared. The computations were stopped when the L_2 norm of the residuals was reduced 12 orders of magnitude. In Table 3, the number of *V*-cycles for each multigrid level, the total number of *V*-cycles and the total CPU-time are listed. For this test case, once the finest grid solution is reached, i.e. the VMG2 cycle is used and the SV2 scheme solution is computed, the coarse grid solution takes 69% of the total CPU-time listed in Table 3. The superscript $*$ indicates that the residuals are not yet converged. In fact, after $10,000^*$ *V*-cycles the E-RK scheme reduced the L_2 norm of the residuals by 9 orders of magnitude. From this table it is seen that the LU-SGS + BE scheme is more than one order of magnitude faster than the E-RK scheme in terms of CPU-time.

In order to study the convergence properties of the LU-SGS + BE solver, this test case was also computed on a grid with 5440 triangular cells with $AR_{max} = 162$. Table 2 shows also the CFL number used for this new mesh. Note that the power law of the CFL number and its maximum value for LU-SGS + BE scheme is exactly the same as used for the mesh with $AR_{max} = 2$.

Fig. 18 shows the convergence histories of the continuity equation of the E-RK and LU-SGS + BE schemes for this mesh. In Table 3, the number of *V*-cycles for each multigrid level, the total number of *V*-cycles and the total CPU-time are listed. It is observed that whereas the convergence of the E-RK scheme is significantly slowed down because of the increased AR_{max}, this is not the case for the LU-SGS + BE scheme. The required number of *V*-cycles to reduce the residual 12 orders of magnitude (495 *V*-cycles) is almost identical as for the $AR_{max} = 2$ case (479 *V*-cycles). In Table 4 the drag coefficients c_d for both simulations are summarized. Good agreement with the experimental data [34] is found.

To conclude this study on the cylinder, the effect of the low Mach number on the convergence rate of the LU-SGS + BE solver is presented. In Fig. 19, the convergence histories of the continuity equation of the LU-SGS + BE scheme for both meshes ($AR_{max} = 2$ and $AR_{max} = 162$) are shown for three values of the Mach number: 0.15, 0.05, 0.005. The Reynolds and

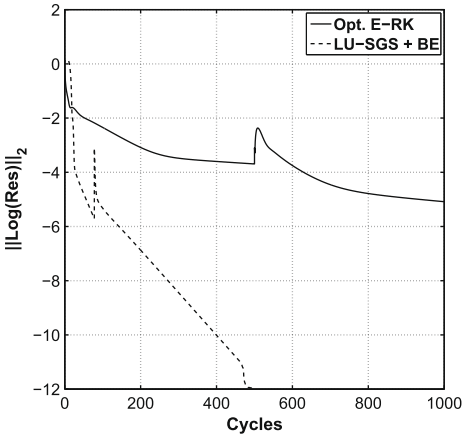

Fig. 17. Convergence histories of E-RK scheme and LU-SGS + BE scheme applied to subsonic laminar cylinder flow. SV2 scheme, unstructured grid with 3744 cells, $AR_{max} = 2$.

Table 3
Number of V-cycles and total CPU-time of E-RK scheme and LU-SGS + BE scheme applied to subsonic laminar cylinder flow. SV2 scheme. Unstructured grids with 3744 cells, $AR_{max} = 2$, and 5440 cells, $AR_{max} = 162$.

	Scheme	VMG1	VMG2	Total VMG	Total CPU-time (s)
$AR_{max} = 2$	Opt. explicit R–K	500	9500*	10,000*	145,094*
	LU-SGS + BE	78	401	479	17,576
$AR_{max} = 162$	Opt. explicit R–K	500	9500*	10,000*	211,859*
	LU-SGS + BE	77	418	495	24,861

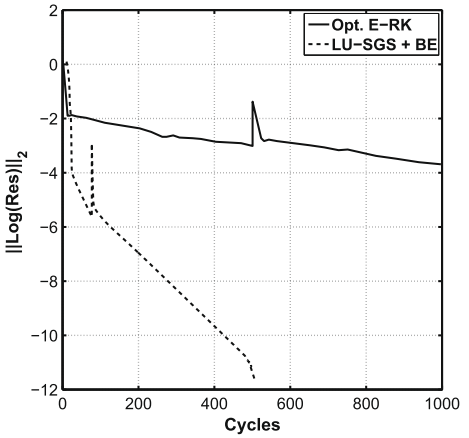

Fig. 18. Convergence histories of the E-RK scheme and the LU-SGS + BE scheme applied to subsonic laminar cylinder flow. SV2 scheme, unstructured grid with 5440 cells, $AR_{max} = 162$.

Table 4
Drag coefficient for subsonic laminar cylinder flow computed with the LU-SGS + BE scheme.

	Experimental data [34]	LU-SGS + BE $AR_{max} = 2$	LU-SGS + BE $AR_{max} = 162$
c_d	1.536	1.526	1.531

Prandtl numbers were again fixed to 40 and 0.72, respectively. The power law of the CFL number and its maximum value for LU-SGS + BE scheme is the same as used for the mesh with $AR_{max} = 2$ and $AR_{max} = 162$. The computations were stopped when the L_2 norm of the residuals was reduced 12 orders of magnitude. In Table 5 the number of V-cycles for each multigrid level and the total number of V-cycles for the three values of the Mach number are listed. In these tables, two values for the total number of V-cycles are indicated. The first one is the total number to reduce the L_2 norm of the residuals 10 orders of magnitude, while the second one is the total number for 12 orders of magnitude. It is seen that with both meshes, the required number of V-cycles to transfer the solution from a first-order polynomial approximation to a second-order polynomial approximation (VMG1) decreases when the Mach number is reduced. The switch to a finer level is made when the L_2 norm of the coarse level residuals is smaller η_{switch} times the L_2 norm of the fine level residual. In the present work the parameter is η_{switch} is set to 0.001.

Furthermore, Fig. 19 shows that the convergence rate of the LU-SGS + BE method for a residual norm higher than 10^{-11} is not slowed by a decrease of the Mach number. On the contrary, for $M = 0.005$, the required number of V-cycles to reduce the residual norm 10 orders of magnitude is smaller than the computation with $M = 0.15$. The low Mach number, combined with a mesh with high-aspect ratio, slightly affected the convergence rate of the LU-SGS + BE solver. For $M = 0.005$ and the mesh with $AR_{max} = 162$, the LU-SGS + BE scheme took 34 V-cycles more than that for the mesh with $AR_{max} = 2$. For a residual norm smaller than 10^{-11} the convergence rate of the LU-SGS + BE solver slows. This behavior is caused by roundoff errors which are more influential at low Mach number.

8.2. Laminar flow around a NACA0012 airfoil

The compressible laminar flow simulation over a NACA0012 airfoil was conducted at free-stream Mach number of 0.5, Reynolds number based on the airfoil chord of 5000 and Prandtl number of 0.72. A grid with 6878 triangular cells with

2
0
−2
−4
−6
−8
−10
$||Log(Res)||_2$

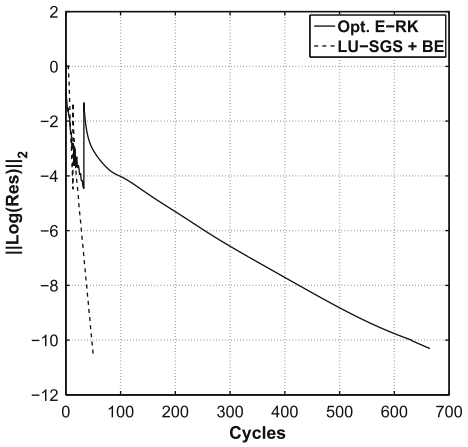

Fig. 20. Convergence histories of the E-RK scheme and the LU-SGS + BE scheme applied to subsonic laminar flow over a NACA0012 airfoil at zero angle of attack. SV2 scheme, unstructured grid with 6878 cells, $AR_{max} = 2.5$.

Table 7
Number of *V*-cycles and total CPU-time of the E-RK scheme and the LU-SGS + BE scheme applied to subsonic laminar flow over a NACA0012 airfoil at zero angle of attack. SV2 scheme, unstructured grid with 6878 cells, $AR_{max} = 2.5$.

Scheme	VMG1	VMG2	Total VMG	Total CPU-time (s)
Opt. E-RK	35	606	641	16,589
LU-SGS + BE	13	49	62	2784

ulations have a different number of degree of freedom (DOF): the SV2 scheme for two-dimensional problems has six times the number of DOF of a classical FV scheme [7–13]. For that reason and because the simulations were done on different computers, no CPU-time comparisons will be shown. The same conditions as in the previous computation are used except for the angle of attack which is set to 2.5°.

The RK3/implicit scheme uses a structured quadrilateral mesh while the LU-SGS + BE scheme uses a triangular mesh constructed from the quadrilateral mesh. A mesh with 16384 quadrilateral cells or 32768 triangular cells and a $AR_{max} = 136$ was used. In the calculation of the RK3/Implicit Residual the CFL number was 16 during the first 8 multigrid cycles and then, it was increased to 10^3. For the LU-SGS + BE scheme the CFL number was set to 10^6 during the entire calculation. In Fig. 22, the convergence histories of the continuity equation of the RK5 Standard code, the RK3/Implicit Residual and the LU-SGS + BE scheme are compared. In Table 8 the total number of *V*-cycles are listed. We see that LU-SGS + BE requires 19 cycles more than the RK3/Implicit Residual code and nearly one order of magnitude less than the RK5 Standard code. In terms of multigrid cycles, the RK3/Implicit Residual scheme is more efficient than the LU-SGS + BE scheme. However, the work per DOF of the RK3/Implicit Residual scheme is approximately twice that of the LU-SGS + BE scheme. The RK3/Implicit Residual scheme employs 12 point-wise SGS (3 SGS sweeps plus a residual calculation times three RK stages) per DOF, while the LU-SGS + BE scheme requires only 6 SGS sweeps per DOF. However, the LU-SGS + BE scheme requires the computation of the

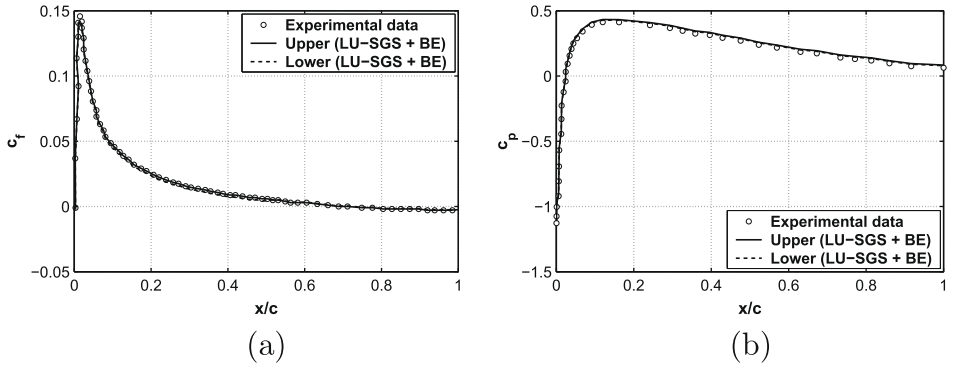

Fig. 21. Distribution of the skin friction coefficient (a) and pressure coefficient (b) on the NACA0012 airfoil surface computed with the implicit the LU-SGS + BE scheme. SV2 scheme, unstructured grid with 6878 cells, $AR_{max} = 2.5$.

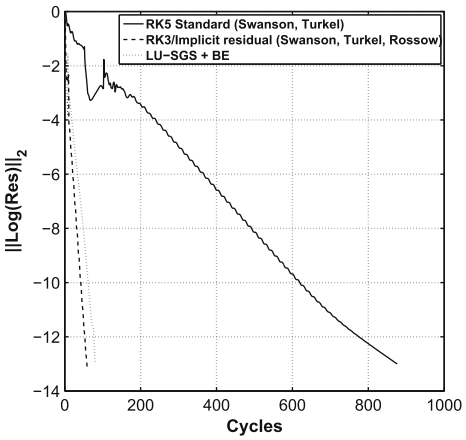

Fig. 22. Convergence histories of the RK3/Implicit residual scheme and the LU-SGS + BE scheme applied to subsonic laminar flow over a NACA0012 airfoil at an angle of attack $= 2.5^{\circ}$. 2nd-order FV scheme/SV2 scheme, structured quadrilateral/unstructured triangular grid, $AR_{max} = 136$.

Table 8
Number of *V*-cycles of the RK5 Standard scheme, the RK3/Implicit Residual scheme and the LU-SGS + BE scheme applied to subsonic laminar flow over a NACA0012 airfoil at an angle of attack 2.5°. 2nd-order FV/SV scheme, structured quadrilateral/unstructured triangular grid, $AR_{max} = 136$.

Scheme	Total number of cycles
RK5 Standard	773
RK3/Implicit Residual	58
LU-SGS + BE	77

Table 9
Drag coefficient for subsonic NACA0012 flow at an angle of attack = 2.5° computed with RK5 Standard scheme, RK3/Implicit Residual scheme and the LU-SGS + BE scheme.

Scheme	c_d	c_l
RK5 Standard	0.0568425	0.0331927
RK3/Implicit Residual	0.0568523	0.0333319
LU-SGS + BE	0.0562196	0.0331650

LHS of Eq. (17), which is time-consuming since its size is quite large. The total number of diagonal block matrix elements that have to be stored for a tetrahedral mesh with N^{SV} cells with polynomial degree p increases with p^4 in 2D and p^6 in 3D. Finally, in Table 9 the drag coefficient (c_d) and the lift coefficient (c_l) for the three simulations are summarized. The table shows good agreement between the results of the three codes.

9. Conclusions

The stability and the smoothing properties of the implicit lower–upper symmetric Gauss–Seidel algorithm with the backward Euler scheme, in combination with the 2D spectral volume schemes and an upwind Riemann flux have been studied, based on the Von Neumann analysis of the 2D linear convection equation. The Von Neumann analysis has been performed for a CFL number of 10^6 and on two meshes with low- and high-aspect ratio to show the effects of the number of symmetric Gauss–Seidel sweeps on the amplification factor. The analysis has demonstrated that the implicit lower–upper symmetric Gauss–Seidel algorithm with the backward Euler scheme is always stable for any choice of the convective velocity direction and the solution orientation for second-order spectral volume schemes. Furthermore, the analysis has shown that the smoothing properties of the implicit solver depend strongly on the orientation of the solution and on the CFL number.

Several test cases have been used to study the damping behavior of the implicit iterative scheme. It is seen that increasing the number of the SGS sweeps the damping behavior of the lower–upper symmetric Gauss–Seidel algorithm with the backward Euler scheme gets closer to the damping properties of a direct solver with backward Euler scheme. Moreover, it has been shown that for the 2D linear convection equation, 5 SGS sweeps are enough to get good damping of the high-frequency error components for a CFL number of 10^6.

We see that the amplification factor may have a discontinuity for a certain wave number. This depends on the direction of the harmonic wave solution and the number of SGS sweeps employed. Nevertheless, the high-frequency error components

are always well damped. Besides, for a specific direction of the harmonic wave solution ($\theta = 0$) of the 2D linear convection equation, the implicit iterative scheme shows an amplification factor which is close to 1 for a wave number range equal to half of the period of the numerical dispersion relation. For wave numbers higher than half the period the amplification factor is close to 0.

The performance of the implicit nonlinear LU-SGS scheme has been evaluated by solving the 2D, laminar Navier–Stokes equations for the flow over a cylinder and a NACA0012 airfoil. In all test cases a CFL number of 10^6 and 6 SGS sweeps have been used and the effect of the mesh aspect ratio on the convergence rate has been investigated. From the Von Neumann analysis for the 2D linear convection equation it was found that a maximum number of 5 SGS sweeps are in general sufficient to get good damping of the high-frequency error components for a CFL number of 10^6. The numerical results show that the convergence behavior of the implicit scheme is not greatly affected by the cell aspect ratio of the mesh. Furthermore, for the flow over a cylinder, the effect of the Mach number on the convergence rate of the implicit lower–upper symmetric Gauss–Seidel algorithm with the backward Euler scheme has been studied. The analysis has demonstrated that the implicit solver is slightly affected by the low Mach number when meshes with isotropic cells are employed. For meshes with anisotropic cells and high-aspect ratio, the effects of the low Mach number are clearly visible.

With the implicit scheme and the *p*-multigrid strategy the computational time can be reduced by a factor of up to 5–10 for laminar flows as compared to a well tuned E-RK scheme. The convergence rate of the implicit LU-SGS scheme on the NACA0012 airfoil test case is comparable with that of a very efficient reference code [21]. In addition, this implicit LU-SGS algorithm requires less memory than classical implicit approaches because only the block matrices on the diagonal of the system matrix have to be stored.

Acknowledgment

This research was funded by IWT under Project SBO 050163. This funding is gratefully acknowledged.

References

[1] B. Cockburn, C.-W. Shu, TVB Runge–Kutta local projection discontinuous Galerkin finite element method for conservation laws II: general framework, Mathematics of Computation 52 (1989) 411–435.
[2] B. Cockburn, S.-Y. Lin, C.-W. Shu, TVB Runge–Kutta local projection discontinuous Galerkin finite element method for conservation laws III: one-dimensional systems, Journal of Computational Physics 84 (1989) 90–113.
[3] B. Cockburn, S. Hou, C.-W. Shu, TVB Runge–Kutta local projection discontinuous Galerkin finite element method for conservation laws IV: the multidimensional case, Mathematics of Computation 54 (1990) 545–581.
[4] B. Cockburn, C.-W. Shu, The Runge–Kutta discontinuous Galerkin method for conservation laws V: multidimensional systems, Journal of Computational Physics 141 (1998) 199–224.
[5] B. Cockburn, C.-W. Shu, The local discontinuous Galerkin method for time-dependent convection–diffusion systems, SIAM Journal of Numerical Analysis 35 (6) (1998) 2440–2463.
[6] M. Ricchiuto, A. Csík, H. Deconinck, Residual distribution for general time-dependent conservation laws, Journal of Computational Physics 209 (2005) 249–289.
[7] Z.J. Wang, Spectral (finite) volume method for conservation laws on unstructured grids: basic formulation, Journal of Computational Physics 178 (2002) 210–251.
[8] Z.J. Wang, Y. Liu, Spectral (finite) volume method for conservation laws on unstructured grids II: extension to two-dimensional scalar equation, Journal of Computational Physics 179 (2002) 665–697.
[9] Z.J. Wang, Y. Liu, Spectral (finite) volume method for conservation laws on unstructured grids III: one-dimensional systems and partition optimization, Journal of Scientific Computing 20 (2004) 137–157.
[10] Z.J. Wang, L. Zhang, Y. Liu, Spectral (finite) volume method for conservation laws on unstructured grids IV: extension to two-dimensional Euler equations, Journal of Computational Physics 194 (2) (2004) 716–741.
[11] Y. Liu, M. Vinokur, Z.J. Wang, Spectral (finite) volume method for conservation laws on unstructured grids V: extension to three-dimensional systems, Journal of Computational Physics 212 (2006) 454–472.
[12] Y. Sun, Z.J. Wang, Y. Liu, Spectral (finite) volume method for conservation laws on unstructured grids VI: extension to viscous flow, Journal of Computational Physics 215 (2006) 41–58.
[13] Z.J. Wang, Y. Liu, Extension of the spectral volume method to high-order boundary representation, Journal of Computational Physics 211 (2006) 154–178.
[14] K. Van den Abeele, T. Broeckhoven, C. Lacor, Dispersion and dissipation properties of the 1D spectral volume method and application to a *p*-multigrid algorithm, Journal of Computational Physics 224 (2) (2006) 616–636.
[15] K. Van den Abeele, C. Lacor, An accuracy and stability study of the 2D spectral volume method, Journal of Computational Physics 226 (2007) 1007–10026.
[16] A. Brandt, Guide to Multigrid Development, Springer, Berlin, 1982.
[17] Y. Liu, M. Vinokur, Z.J. Wang, Spectral difference method for unstructured grids I: basic formulation, Journal of Computational Physics 216 (2006) 780–801.
[18] G. May, A. Jameson, A spectral difference method for the Euler and Navier–Stokes equations on unstructured meshes, in: 44th AIAA Aerospace Sciences Meeting Reno, Nevada, January 2006.
[19] Z.J. Wang, Y. Liu, G. May, A. Jameson, Spectral difference method for unstructured grids II: extension to the Euler equations, Journal of Scientific Computing 32 (1) (2007) 449–454.
[20] H. Bijl, M.H. Carpenter, V.N. Vatsa, Time integration schemes for the unsteady Navier–Stokes equations, AIAA Paper 2001–2612, 2001.
[21] R.C. Swanson, E. Turkel, C.-C. Rossow, Convergence acceleration of Runge–Kutta schemes for solving the Navier–Stokes equations, Journal of Computational Physics 224 (2007) 365–388.
[22] A. Jameson, E. Turkel, Implicit schemes and LU decompositions, Mathematics of Computations 37 (1981) 385–397.
[23] A. Jameson, S. Yoon, Lower–upper implicit schemes with multiple grids for the Euler equations, AIAA Journal 25 (7) (1987) 929–935.
[24] Y. Sun, Z.J. Wang, Y. Liu, C.-L. Chen, Efficient implicit LU-SGS algorithm for high-order spectral difference method on unstructured hexahedral grids, in: 45th AIAA Aerospace Sciences Meeting, Reno, Nevada, January 2007.
[25] P.E.O. Buelow, S. Venkateswaran, C.L. Merkle, Stability and convergence analysis of implicit upwind schemes, Computer and Fluids 30 (2001) 961–988.

[26] J.S. Kim, O.K. Kwon, Assessment of implicit operators for the upwind point Gauss–Seidel method on unstructured meshes, Computer and Fluids 36 (2007) 1335–1346.
[27] M. Parsani, K. Van den Abeele, C. Lacor, Implicit LU-SGS time integration algorithm for high-order spectral volume method with *p*-multigrid strategy, in: West-East High-Speed Flow Field Conference, Moscow, Russia, November 2007.
[28] P.D. Lax, Weak solutions of non-linear hyperbolic equations and their numerical computation, Communications on Pure and Applied Mathematics VII (1954) 159–193.
[29] P.L. Roe, Approximate Riemann solvers parameter vectors and difference scheme, Journal of Computational Physics 43 (1981) 357–372.
[30] A. Quarteroni, R. Sacco, F. Saleri, Numerical Mathematics, Springer, Berlin, 2002.
[31] B.T. Helenbrook, H.L. Atkins, Application of *p*-multigrid to discontinuous Galerkin formulations of the Poisson equation, AIAA Journal 44 (3) (2005) 566–575.
[32] D. Sharov, N. Nakahashi, Reordering of hybrid unstructured grids for lower–upper symmetric Gauss–Seidel computations, AIAA Journal 36 (3) (1998) 484–486.
[33] C. Geuzaine, J.-F. Remacle, Gmsh: a three-dimensional finite element mesh generator with built-in pre- and post-processing facilities, International Journal for Numerical Methods in Engineering 79 (11) (2009) 1309–1331.
[34] J.B. Barlow, W.H. Rae, A. Pope, Low-Speed Wind Tunnel Testing, Jhon Wiley & Sons, Canada, 1999.
[35] Experimental data base for computer program assessment, AGARD AR-138, May, 1979.